EVALUATING ATMOSPHERIC CORRECTION METHODS USING WORLDVIEW-3 IMAGE
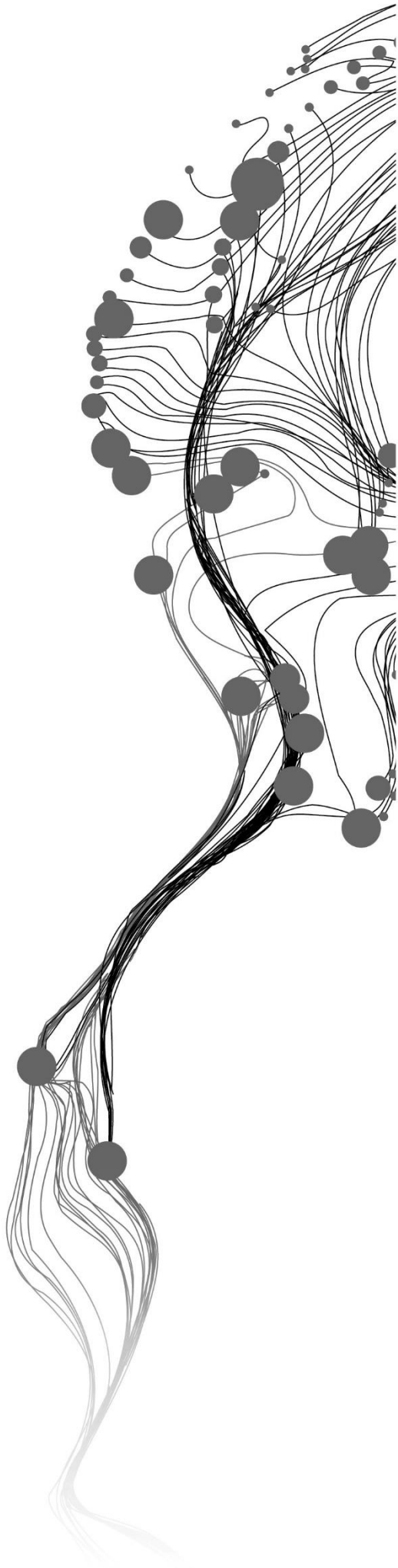
AMARJARGAL DAVAADORJ
February, 2019

SUPERVISORS:
W.H. Bakker MSc
Dr. H.M.A van der Werff

EVALUATING ATMOSPHERIC CORRECTION METHODS USING WORLDVIEW-3 IMAGE

AMARJARGAL DAVAADORJ
Enschede, The Netherlands, February, 2019

ABSTRACT

This research presents an evaluation of various atmospheric correction (AC) methods applied to WorldView-3 (WV-3) high resolution multispectral image. Numerous studies have been conducted to evaluate the performance of AC methods using hyperspectral and multispectral datasets for various land surfaces and environments. However, an assessment of AC methods using WV-3 multispectral image with the help of ground spectral data has not been done yet. The aim of this study is to determine the most suitable atmospheric correction method for WV-3 satellite images by evaluating different methods of AC. The WV-3 images used in this research were acquired in May and September 2017, over Rodalquilar, the epithermal gold deposit- located in the southeast of Spain. The study also used field spectral data collected in Rodalquilar by ITC staff in September 2017.

In this research, two modules of ATCOR (ATCOR2 and ATCOR3) and FLAASH AC methods were applied to WV-3 images with three different aerosol models. The results of the AC methods were compared separately within each method with different aerosol models. Once the optimal aerosol type was defined, comparisons were done between the AC methods and between the two scenes. DigitalGlobe's AComp atmospherically corrected reflectance images from the same dates were also added to the AC comparisons. Lastly, two sets of band ratios and the Spectral Angle Mapper (SAM) were used to map alteration minerals of the study area.

From the results, the maritime aerosol model found to be the optimal aerosol model for the study area, and the urban aerosol model appeared to overestimate the reflectance. Each of the AC methods did show some unknown features at different wavelengths which are recommended to investigate further. Mineral mapping results from the band ratio techniques showed an overall good correlation between the FLAASH and AComp outcomes, although they differed in the value range and were affected by the striping. Mineral maps produced by using SAM showed differences in mineral abundances as well as, spatial distributions. Comparisons and evaluation of AC methods and mineral mapping results were not straightforward due to different versions of datasets, striping effect, geolocation differences, and different approaches of field measurements. We expect this research to contribute its value to the understanding of potential issues and sources of errors in processes of AC and image analysis techniques and the selection of suitable AC method for WV-3 image. Overall, we found the FLAASH method to be the superior over the other methods used in this study.

ACKNOWLEDGEMENTS

TABLE OF CONTENTS

LIST OF FIGURES

LIST OF TABLES

LIST OF APPENDICES

1. INTRODUCTION

1.1. Research background

In optical remote sensing image analysis, conversion of at-sensor radiance values into reliable surface reflectance data is key for identification and mapping of mineral composition of the surface. Radiance measured at sensor represents only relative brightness values of the target surface due to effects of the Earth's atmosphere, sun illumination, topography, etc. (Gupta, 2018, p. 115). Water vapours, aerosols, and gases contained in the Earth's atmosphere absorb and scatter solar radiation, thus affecting reflected radiation from the Earth and change the radiation received by the satellite sensor. To account and remove atmospheric influences from the image it is required to perform atmospheric corrections in the pre-processing stage of the image analysis.

Atmospherically corrected surface reflectance data is important for many aspects: 1- the shapes of reflectance spectra are indications of chemical and physical properties of the surface materials; 2- reflectance spectra can be compared with ground and laboratory spectra; 3- reflectance data can be analyzed for quantitative change detection evaluation (Clark et al., 2002; Gupta, 2018, p. 115). An artefact in spectral shape caused by poor atmospheric correction may be interpreted as a false anomaly, and its investigation could lead to a waste of time and money (Clark et al., 2002). Therefore, well-calibrated reflectance data has greater validity and confidence in providing realistic surface properties and consequently- result in accurate surface compositional maps.

Generally, approaches for atmospheric corrections can be divided into two main groups: empirical methods and model based methods. Earlier studies include several empirical methods, such as dark object subtraction (DOS), empirical line (EL) calibration, flat field (FF) calibration method and internal average relative reflectance (IARR) (B. C. Gao et al., 2009). These empirical methods are scene-based, except EL, which requires in-situ reflectance measurements of bright and dark target areas in the site. In addition, empirical methods provide only relative surface reflectance while RTM based methods perform absolute calibration of remote sensing image with higher accuracy (Gupta, 2018, p. 119). Considering this major difference between the two groups of methods, this research focused on the RTM based atmospheric correction methodology.

RTM methods are based on complex theoretical modelling of the atmospheric absorption and scattering by water vapours, aerosols and gases and, thus they require data on atmospheric conditions at the time of image acquisition (Kale et al., 2017). According to Ben-Dor et al. (2004), users tend to move to RTM methods because it provides reasonable results and does not require a field visit. Radiative transfer models named as LOWTRAN, MODTRAN, HITRAN, 5S and 6S are all reference models (Tempfli et al., 2009) and they are used for basic calculations in atmospheric correction software packages. Some of the software packages are: ATREM (B.-C. Gao & Davis, 1997) and HATCH (Qu et al., 2003) are developed based on 5S and 6S models, while ATCOR (Richter & Schläpfer, 2002), ACORN (Miller, 2002) and FLAASH (Perkins et al., 2012) are based on MODTRAN model.

All above-stated AC methods have been compared and evaluated by numerous researchers, and their advantages and limitations were discussed in several studies. For instance, RTM methods' performance were compared and evaluated using hyperspectral datasets such as AVIRIS and Hyperion (Ben-Dor et al., 2004; Goetz et al., 2003; Kruse, 2004; San & Suzen, 2010; Kawishwar, 2007). AC methods have been evaluated also in terms of suitability for specific type of land surface or environment, such as for playa environment (Ayoobi & Tangestani, 2017), soil-vegetation mixed environment (Ben-Dor et al., 2004), urban coastal environment (Nazeer et al., 2014) and for forested regions (Janzen et al., 2006).

Furthermore, AC methods were compared and assessed for specific satellite data types, e.g. Landsat, SPOT, IKONOS, QuickBird and WorldView-2 (Manakos et al., 2011). But, for the WorldView-3 satellite image, performance of different atmospheric correction methods has not been assessed yet.

WorldView-3 (WV-3) is a high spatial resolution commercial multispectral satellite sensor operating at an altitude of 617km, launched in August 2014. DigitalGlobe's WV-3 has panchromatic band with 31cm resolution, eight bands with 1.24m spatial resolution in the visible to near-infrared (VNIR) region from 427.4nm to 913.6nm and eight bands with 3.7m spatial resolution in shortwave infrared (SWIR) region covering the spectral range of 1209.1nm to 2329.2nm (Kuester, 2016). The SWIR bands are well placed in the key wavelength positions of diagnostic absorption features of Al-OH (2.16-2.2μm), Mg-OH (2.3-2.36μm), Fe-OH (2.23-2.3μm) bearing alteration minerals and carbonate minerals (2.3-2.35 μm) (Sun et al., 2017). Thus WV-3 provides new mineral mapping capabilities that are not available for other operational multispectral satellite sensors such as Landsat-8 and Sentinel-2 which have only two broad SWIR bands. Also, ASTER SWIR sensor has failed since April 2008 and other WorldView satellites do not have SWIR bands.

In recent years, the WV-3 has received much attention on its evaluation of potentials in geologic and other geoscientific fields. The SWIR bands' geologic potentials were evaluated and demonstrated before and after the launch of the WV-3 satellite, using simulated and acquired data from space in Cuprite, Nevada (Kruse & Perry, 2013; Kruse et al., 2015). Other studies were carried out by Sun et al. (2017) and Ye et al. (2017) using combined VNIR and SWIR bands for alteration and lithological mapping with a comparison of ASTER and OLI/Landsat-8 data in Pobei area, China. The most recent study was an MSc thesis conducted by Usman (2018) who compared mineral mapping capabilities of WV-3 and ASTER data in an epithermal alteration system – Rodalquilar in Spain.

To the best of knowledge, a study about the comparison of AC methods using ground validation has never been applied to the WV-3 data. Thus, it remains unclear which of the various atmospheric correction methods works best for the WV-3 data. These different AC methods then need to be evaluated for obtaining the best output result from WV-3 data.

The current research focused on evaluating different RTM atmospheric correction methods on WV-3 data of Rodalquilar, an epithermal gold deposit located in Rodalquilar caldera complex, south-eastern Spain. The study area Rodalquilar is a 'Cuprite-like' classic sensor calibration site in Europe (Van der Meer et al., 2018) with well-exposed alteration minerals such as alunite, kaolinite, illite, smectite, calcite and iron oxides within five different hydrothermal alteration zones (Arribas et al., 1995).

1.2. Research objectives

The main objective of this research is to derive the most suitable atmospheric correction method for high spatial resolution multispectral WV-3 data by evaluating various atmospheric correction (AC) methods. The following sub-objectives are set, and several research questions are raised in order to achieve the main objective.

Sub-objectives:
1. To investigate the effects of different RTM based AC methods on derived reflectance by testing atmospheric input parameters separately.
2. To compare and analyse the differences in derived reflectance from each of the AC methods with in-situ measurements.
3. To evaluate the differences in mineral maps produced from the output of various AC methods.

1.3. Research questions

1. What are the most influential atmospheric parameters and software settings that cause differences in derived reflectance for each AC method?
2. Which spectral region has the most variations in absorption features of reflectance spectra derived from each method?
3. How much do mineral mapping results change due to different atmospheric correction methods?
4. What is the optimal way to validate image data with field spectral data which has different spatial resolution and areal coverage compared to the image pixel?

1.4. Study area and dataset

1.4.1. Location and geology of the study area

The Rodalquilar study area is located in the 40km east of the capital of the province Almeria, southeast Spain. Rodalquilar is chosen as a study area based on several reasons: 1) the area hosts different hydrothermal alteration zones consisting of VNIR and SWIR active minerals; 2) data availability; 3) it has been used as a sensor calibration test site in many studies; 4) it is a semi-arid region which is appropriate for geologic remote sensing geologic study due to scarce vegetation cover.

The Rodalquilar epithermal gold deposit is located in Rodalquilar caldera complex within the Cabo de Gata volcanic field along the south-eastern coast of Spain (Figure 1). The volcanic field extends for 40km along the Mediterranean Sea and consists of Miocene calc-alkalic volcanic rocks and andesitic stratovolcanoes and cones (Rytuba et al., 1990; Oyarzun et al., 2009).
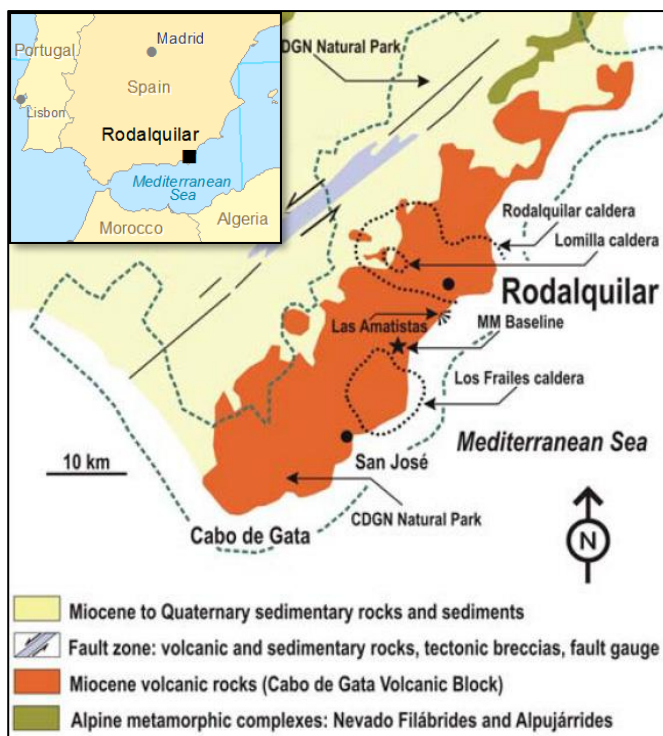
Figure 1. Location of the study area and the geologic map of the Cabo de Gata volcanic field modified after Oyarzun et. al. (2009)

The Rodalquilar caldera complex is composed of two nested calderas. The outer one is the Rodalquilar caldera, and the inner one is the Lomilla caldera (Figure 1). In this caldera complex, volcanic activities such as eruption, caldera collapse, and resurgence happened multiple times, and as a result, the area covered by different lithological units and hydrothermal alteration zones. The geology, alteration and mineralisation of the area are well studied and documented (Arribas et al., 1995; Oepen et al., 1989; Rytuba et al., 1990).

Figure 2 shows a detailed geologic map of the area created by Arribas (1993). The oldest unit in this complex is Precaldera andesitic rock, and overlying units are rhyolitic Cinto ash-flow tuff, rhyolite ring domes, and the Las Lazaras ash-flow tuff. The emplacement of porphyritic hornblende andesite rocks caused the evolution of the hydrothermal system and the epithermal gold deposit. This unit was intruded by pyroxene andesite dykes. The youngest units are thick marine sediments, consisting of fossiliferous limestone and sandstone in the eastern and western margins of the caldera complex (Arribas et al., 1995). In Rodalquilar the following alteration zones are present: propylitic, sericitic, intermediate argillic, advanced argillic and silicic (Arribas et al., 1995; Oepen et al., 1989). Dominant alteration minerals present in these zones are silica, alunite, kaolinite, dickite, illite, illite-smectite, pyrophyllite, chlorite, pyrite, k-feldspar, plagioclase, hematite, goethite, and jarosite (Arribas et al., 1995).
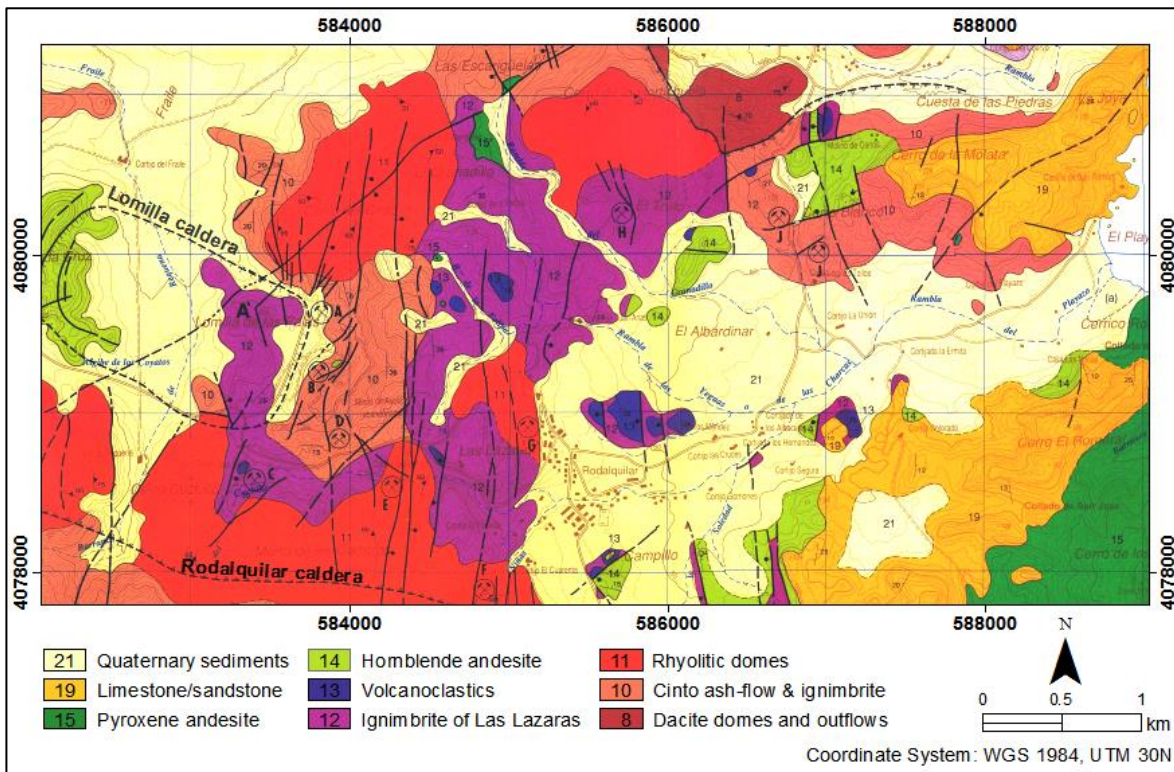
Figure 2. 1:25000 scale geologic map of Rodalquilar by Arribas (1993). The legend is taken and modified from Van der Werff & Van der Meer (2016).

1.4.2. Satellite data

The datasets used in this research were WorldView-3 (WV-3) multispectral high resolution satellite images of two scenes acquired in May and September 2017. The September dataset has two different versions: the original and recalibrated. The recalibrated September images were obtained after encountering a striping effect in the late stage of the research and used for only mineral mapping processes. The original datasets consist of two different products radiance-at sensor and the surface reflectance images while the recalibrated dataset includes only radiance-at sensor images. Details of the datasets are given in Table 1. The reflectance product is named AComp image and processed to the surface reflectance by DigitalGlobe Inc.

Table 1. WV-3 datasets used in the study.

Dates	12 May 2017		28 September 2017			
Versions	(the original)		(the original)		(recalibrated)	
Product type	Radiance-at sensor	Reflectance (AComp)	Radiance-at sensor	Reflectance (AComp)	Radiance-at sensor	Reflectance (AComp)
Panchromatic image	yes	yes	yes	yes	yes	no
Multispectral VNIR image	yes	yes	yes	yes	yes	no
Multispectral SWIR image	yes	yes	yes	yes	yes	no

All the images are a level 3D orthorectified images the coordinate system of which is UTM projection, zone 30N with WGS 84 datum. Each dataset includes a panchromatic image with a spatial resolution of 0.31m, a multispectral image with eight bands in VNIR region and a multispectral image with eight bands in SWIR regions. Spectral band details are shown in Table 2.

Table 2. The WorldView-3 satellite image band specifications (DigitalGlobe, 2019).

WorldView-3	VNIR bands	Wavelength range	Central wavelength	SWIR bands	Wavelength range	Central wavelength
Spectral bands	Coastal:	400-450nm	427.4nm	SWIR-1:	1195 - 1225 nm	1209.1nm
	Blue:	450-510nm	481.9nm	SWIR-2:	1550 - 1590 nm	1571.6nm
	Green:	510-580nm	547.1nm	SWIR-3:	1640 - 1680 nm	1661.1nm
	Yellow:	585-625nm	604.3nm	SWIR-4:	1710 - 1750 nm	1729.5nm
	Red:	630-690nm	660.1nm	SWIR-5:	2145 - 2185 nm	2163.7nm
	Red Edge:	705-745nm	722.7nm	SWIR-6:	2185 - 2225 nm	2202.2nm
	Near-IR1:	770-895nm	824.0nm	SWIR-7:	2235 - 2285 nm	2259.3nm
	Near-IR2:	860-1040nm	913.6nm	SWIR-8:	2295 - 2365 nm	2329.2nm
Number of bands	8			8		
Spatial resolution	1.2m			7.5m		

1.4.3. Field spectral data

This study used field spectral measurements conducted by ITC staff- Rob Hewson and Harald Van der Werff in September 2017, Rodalquilar Spain (Usman, 2018). The spectral data collected from three reference sites were used in this research. The spectra of the sites were collected using ASD FieldSpec3 spectroradiometer with a spectral resolution of 3nm at 700nm and 10nm at 1400nm and 2100nm in the spectral range of 350-2500nm.

Figure 3 shows the locations and names of the reference sites. The site Wp333 located in the north-western part (red box), is named by the GPS waypoint- wp333 and it is a large bare ground area for car parking. The two other sites located in the coastline were named as Wp311 and Wp313-314 based on corresponding GPS waypoint numbers (green box). The surface of Wp311 site is covered by mostly calcareous sandstone or limestone while the Wp313-314 site is a sandy beach. The photos of the sites are shown in Figure 4.
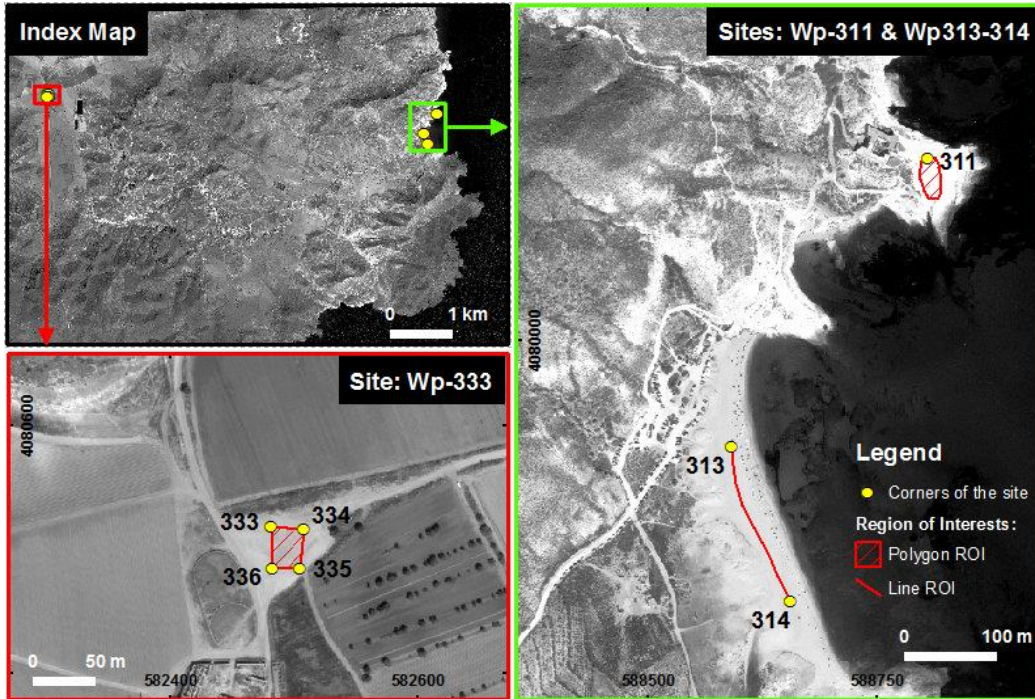
Figure 3. Map showing the locations of the field measurement sites in WV-3 panchromatic image background.

Numerous spectra were collected from each site using two different methods of ASD spectrometer: with bare fibreoptic cable and with contact probe (Table 3). In Wp333, spectra were collected using a bare fibreoptic cable with a field of view (FOV) of an approximately 30cm area on the ground and with 3-4m line spacing in a grid. These measurements have been done between 10 am - 11 am on 12 September 2017, which is the same time of WV-3 image acquisition. Spectra for both Wp-311 and Wp313-314 sites were collected using contact probe measurements on 8-9 September. Descriptions of the sites and measurements are provided in Table 3.

Table 3. Descriptions of the field sites and their spectral measurements done by Hewson and Van der Werff.

Site name	Description of the site	No of spectra	Method	Date
Wp333	Bare ground for parking	110	ASD-bare fibreoptic cable, grid measurements in 3-4 m sampling interval, ~ 30cm FOV.	12 Sept 2017
Wp311	Large exposure of calcareous sandstone/limestone on the promontory, SE of stone fortification (El Playazo beach).	71	ASD-contact probe measurements within ~50m of WP311	8 Sept 2017
Wp313-314	El Playazo beach	50	ASD-contact probe measurements in traverse line	9 Sept 2017

Figure 4 shows the averaged spectral signatures of the sites and their surface photos. The original field spectra were then resampled according to the WV-3 spectral bands for the purpose of comparing and validating the surface reflectance estimated from the WV-3 satellite data.

Spectral profiles of the sites **Photos of the sites**
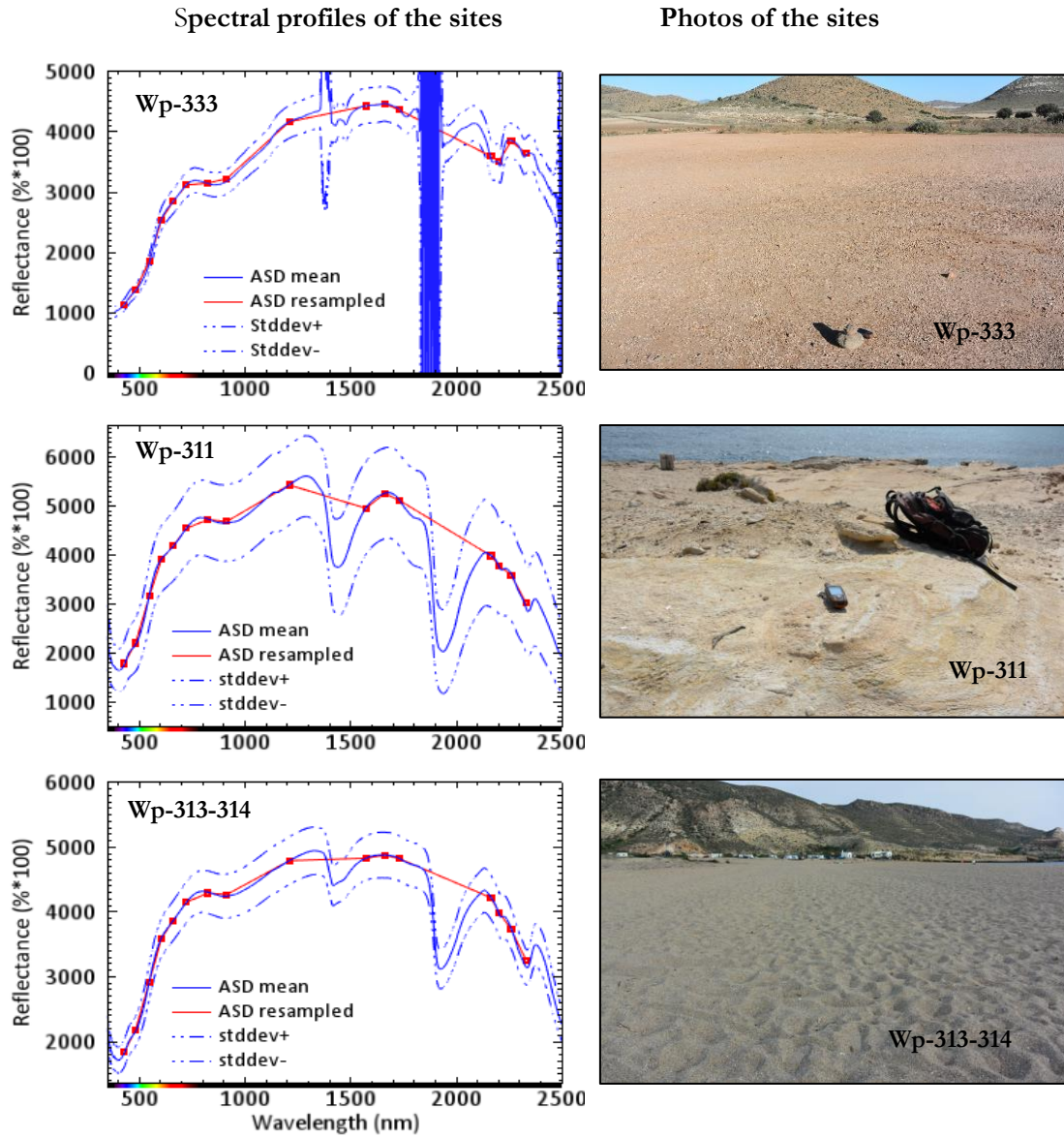
Figure 4. Spectra of the reference sites collected by ITC staff in Rodalquilar, September 2017: measured ASD field spectra (blue) and resampled to WV-3 spectra (red). Photos of the sites are provided on the right. The locations of these sites are shown in Figure 3.

1.4.4. Weather conditions

As stated earlier, RTM based atmospheric correction methods require data on atmospheric conditions when the image is acquired. According to the weather information collected in Almeria, Spain during 1985-2015 by CustomWeather (2019), the annual mean temperature throughout the year is +19°C, and annual rainfall is 38.5mm per year. The hottest month of the year is August (27°C average) and the coldest month is January (13°C average). For this study, weather conditions of the months May and September 2017 are provided as the satellite data were acquired during this period (see section 1.4.2 for datasets). The temperature in May ranges from +16°C to +24°C and precipitation is low 1.3mm while in September, the temperature ranges from +20°C to +28°C and average precipitation is 2.3mm.

Table 4 provides weather conditions in Almeria, Spain on the two dates of WV-3 image acquisitions (CustomWeather, 2019). This was the closest weather station from Rodalquilar which provides information about past weather condition. As shown in the table below, on 28 May 2017, the weather was

windy (17km/h) and sunny with scattered clouds and visibility was 50km. On the other hand, on 12 September 2017, at the time of satellite overpass- 11 am, the weather was sunny with clear skies and 40km of visibility which are preferred conditions for remote sensing imagery.

Table 4. Weather conditions in Almeria, Spain on the dates of WV-3 image acquisitions. The data source is CustomWeather (2019).

Time	Temperature (° C)	Wind (km/h)	Humidity (%)	Pressure (mbar)	Visibility (km)	Weather
28 May 2017						
5:00	23	11	38%	1015	50	Clear
8:00	20	4	85%	1016	40	Partly sunny
11:00	**24**	**17**	**64%**	**1017**	**40**	**Scattered clouds**
14:00	25	30	63%	1016	40	Scattered clouds
17:00	24	20	64%	1016	40	Partly sunny
12 Sep 2017						
5:00	20	6	79%	1012	30	Clear
8:00	20	6	75%	1013	45	Sunny
11:00	**26**	**6**	**59%**	**1014**	**50**	**Sunny**
14:00	26	15	65%	1015	50	Sunny
17:00	27	9	54%	1015	50	Passing clouds

1.4.5. Auxiliary data

In this research, apart from the satellite and the field data, the 1:25000 scale geological map of Rodalquilar (Arribas, 1993) and the alteration map created by Arribas et al. (1995) were used. Elevation data- MDT05 digital terrain model with the 5m resolution was used for atmospheric correction. This data was downloaded from the Spanish National Geographic Information Centre (National Geographic Center (CNIG), 2018).

1.5. Thesis structure

This thesis consists of five chapters:
- Chapter 1, Introduction, provides research background and defines research problem, objectives, and research questions. It introduces study area and datasets used in this research.
- Chapter 2, Methodology, describes the methods carried out during the research from the applying atmospheric corrections, followed by the comparisons of AC results and finally the methods used for mineral mapping.
- Chapter 3, Results, presents the results of each methods.
- Chapter 4, Discussion, discusses the comparison results of AC methods and mineral maps.
- Chapter 5, Conclusions and Recommendations concludes the main findings answering the research questions and gives further recommendations.

2. METHODOLOGY

The current research involved evaluating different atmospheric correction (AC) methods and mapping of mineralogy of Rodalquilar to determine the best AC method for WV-3 data. Two different AC methods ATCOR and FLAASH were applied to WV-3 satellite images. As stated earlier, the WV-3 images were acquired in May and September 2017. The selected AC methods were performed with different aerosol models and compared with the field spectral data. Afterwards, the results of May and September images were also compared to see the consistency of the AC results and seasonal differences' presence. Finally, for the mineral mapping, two methods of image analysis were used: band ratio techniques and classification using SAM (Spectral Angle Mapper) algorithm. Abovementioned methods were summarised and illustrated by a simple flowchart that shows the main steps where these methods were carried out (see Appendix 1). The following subsections will describe each of the used methods in detail.

2.1. Radiative transfer model based atmospheric corrections

Atmospheric correction of the WorldView-3 (WV-3) image was carried out using two different radiative transfer model (RTM) based methods – ATCOR and FLAASH. RTM based atmospheric correction methods perform absolute atmospheric corrections by modelling the atmosphere according to the similar environmental and geographical conditions of the image acquisition time (San & Suzen, 2010). Atmospheric modelling includes correction for absorption by atmospheric gases (H_2O at 0.94, 1.14, 1.38, 1.88μm; CO_2 at 2.01, 2.08μm, O_2 at 0.76mm; and O3, N_2O, CO, CH_4, NO_2 at various wavelengths) over the range 0.4-2.5μm and scattering by atmospheric gaseous molecules (Rayleigh scattering in 0.4-0.7μm) and aerosols (B. C. Gao et al., 2009). Figure 5 illustrates how a radiance image spectrum is converted to a surface reflectance spectrum after applying an atmospheric correction.
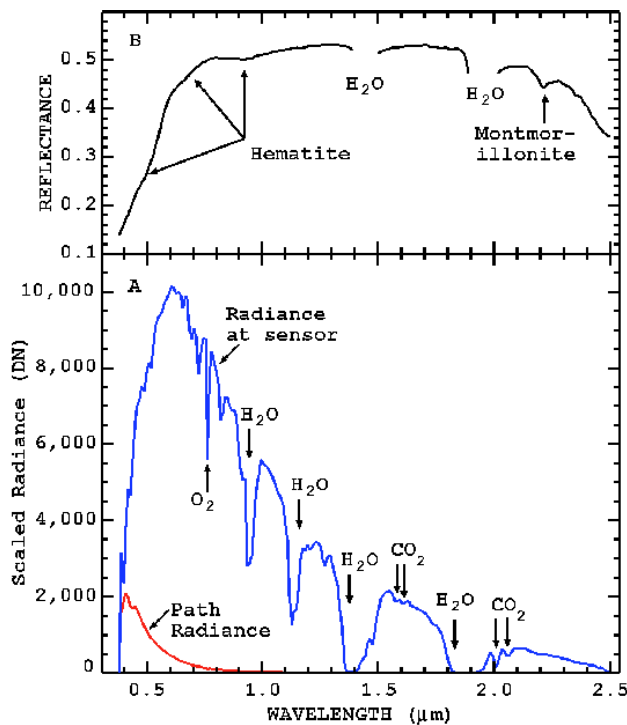
Figure 5. An example of reflectance and radiance spectra. A- radiance spectrum of non-vegetated area and B- the surface reflectance spectrum after atmospheric correction (Clark et al., 2002).

In this figure (A)- a radiance spectrum of the non-vegetated area has a strong influence of solar illumination and absorptions by atmospheric gases. (B)- After atmospheric correction, the spectrum shows absorption features of the minerals (hematite and montmorillonite) on the surface. The water features in

the spectrum A is caused by atmospheric water vapour and water features in the spectrum B are caused by liquid water in the soil (Clark et al., 2002).

Since one of the sub-objectives of this research is to investigate the effects of AC methods, we decided to test different atmospheric condition parameters that rely on the user's selection. According to Richter & Schläpfer (2018), the most important parameters of the atmosphere are the aerosol type, visibility and water vapour amount that vary in space and time. The aerosol type represents a concentration of different aerosol types in the air. It includes absorption and scattering properties of the aerosols and their wavelength dependence properties. The visibility is the maximum horizontal distance at which a human eye can still recognise a dark object (Richter & Schläpfer, 2018). Water vapour amount is the total amount of the gas in the atmospheric column from the ground to the top of the atmosphere, and it is measured as the mass of the water molecules in the atmospheric column over each square cm of the ground surface (Harris Geospatial Solutions, 2018a).

In ATCOR and FLAASH, water vapour amount, aerosol type, and visibility are set by the user. For multispectral sensors that do not have bands in water vapour absorption regions (920-960nm), a constant and standard atmospheric parameter is used for the water vapour. The visibility is set based on the weather conditions (clear sky or hazy) of the imaged day, and the water vapour amount is selected based on the surface temperature, the season of the year and latitude of the locations. In this study, based on the weather conditions of the satellite image acquisitions days, the visibility was chosen as 40km (see 1.4.4 and Table 4). The water vapour amount was selected as $2.92g/cm^2$, same as for the mid-latitude summer season according to the Rodalquilar location and season of the year.

Regarding the aerosol type, both ATCOR and FLAASH have several different aerosol models. In this research three different aerosol models were tested: rural, maritime, and urban. The rural aerosol model represents aerosols in continental areas and is assumed to be composed of 70% of water-soluble substance (ammonium, calcium sulphate and organic compounds) and 30% of dust like aerosol (Abreu et al., 1996). The maritime model is composed of a sea-salt compound and a continental compound which is the rural aerosol type without dust-like compound. The urban model is the same as the rural aerosol type but with the addition of aerosols from combustion products and industrial sources. It is a mixture of 80% of rural type aerosols and 20% of soot-like aerosols (carbonaceous aerosols released from burning fossil fuels, coal, oil and gas) (Abreu et al., 1996). Because Rodalquilar is located in the coastal region, the maritime and the rural models are both applicable depending on the wind direction. If the wind comes from the sea, the maritime would be a good choice, while the wind goes toward the sea then air mass source would be from the continental origin (Richter & Schläpfer, 2018). Therefore, in this research, three different aerosol models were tested to determine the suitable aerosol model for the study area.

FLAASH and ATCOR both use MODTRAN-5 radiative transfer model, but their approaches to calculating surface reflectance differ in detail. MODTRAN in FLAASH calculates first the surface reflectance values at 0, 0.5, and 1.0 for a different range of water vapour column densities, i.e., it performs a forward-modelling (Anderson et al., 1999). Also, they have different functionality such as ATCOR corrects topographic illumination effects using elevation data, whereas FLAASH calculates multiple scattering effects. Details about functions and required input parameters will be provided separately for each method below.

2.2. FLAASH- The Fast Line-of-sight Atmospheric Analysis of Spectral Hypercubes

FLAASH is commercially available as an add-on to the ENVI software, developed by Spectral Sciences, Inc. and the Air Force Research Laboratory (Anderson et al., 1999). It is based on MODTRAN-5 radiative transfer code and operates only in VNIR-SWIR regions up to 3.0μmm not including the longwave infrared region. The basic principle of the FLAASH algorithm is described as below in short. FLAASH calculates image reflectance- ρ using the standard equation for spectral radiance at sensor L:

$$L = \frac{A\rho}{1-\rho_e S} + \frac{B\rho_e}{1-\rho_e S} + L_a \qquad (1)$$

where, ρ_e is a spatially averaged surface reflectance, S is the spherical albedo of the atmosphere (atmospheric reflectance for upwelling radiation), L_a is the radiance backscattered by the atmosphere, and A and B are coefficients that depend on atmospheric and geometric conditions (Anderson et al., 1999; Perkins et al., 2005). The values A, B, S and L_a are determined from MODTRAN simulations of radiance calculated at three different surface reflectance values of 0, 0.5, and 1. The sensor and sun angles, ground elevation, the nominal values for the aerosol type and visibility are used to calculate iteratively for various water profiles to account for possible variations in water vapor. The difference between ρ and ρ_e accounts for the adjacency effect (Perkins et al., 2005). The adjacency effect is a radiance contribution caused by atmospheric scattering that originated from adjacent surfaces not in direct sensor's field of view (Anderson et al., 1999).

2.2.1. Data preparation for FLAASH

FLAASH uses as input data a calibrated radiance image in a floating-point, long integer or integer data type. The WV-3 VNIR and SWIR images from 12 September 2017 were provided in TIFF format with the unsigned integer data type. First, VNIR and SWIR images were stacked together, and here, VNIR data was resampled to a 7.5m resolution of SWIR data pixel size to preserve the original spatial and spectral information of the SWIR bands of WV-3. Because the SWIR bands contain the diagnostic spectral features of the alteration minerals and later, the mineral mapping will be performed based on these bands. This combined data was then transferred into calibrated radiance data using ENVI's 'Radiometric Calibration' tool with a scale factor of 0.1. FLAASH requires input image to be in floating-point data type in units of [μW/ (cm² * sr * nm)]. This scale factor 0.1 converts radiance values from the units of [W/ (m² * sr * μm)] into units of [μW/ (cm² * sr * nm)].

2.2.2. Input parameters required for FLAASH

Scene and sensor information including the scene centre location, the sensor type, and altitude and flight date and time were filled automatically from the header file of the image, except the ground elevation value (Table 5). This value was set to 0.15km according to the average elevation retrieved from DEM-MDT05 of Rodalquilar (see section 1.4.5).

Regarding the atmospheric condition parameters, first, an atmospheric model must be selected by the user from one of the standard atmosphere models according to their water vapour amount. In case of absence of this information, the atmosphere can be selected based on surface air temperature of the area or based on a seasonal-latitude surface temperature model table provided by FLAASH (Harris Geospatial Solutions, 2018a). For this purpose, the water vapour data was obtained from MODIS (Moderate Resolution Imaging Spectroradiometer) Atmosphere product (NASA, 2019). The MODIS/Terra Water Vapour (05_L2) product (MOD05_L2.A2017255.1035.061.2017261085751.hdf) was acquired at 10:35 am on 12 September 2017, the same date of WV-3 image. The water vapour amount was estimated as 2.3g/cm² by averaging the values of the image pixels covering the study area. This amount of water

vapour and latitude of the area and the image acquisition season – September corresponds to the 'Mid-latitude Summer' atmospheric model.

Next, an aerosol model of the atmosphere is selected by the user. As stated earlier in section 2.1, three different aerosol models rural, maritime, and urban were tested to determine the suitable aerosol model for the study area. The visibility was set to 40km according to the weather condition of the day of WV-3 image acquisition- cloud-free and clear skies.

Besides the main input parameters required in the FLAASH, a 'Multispectral setting' is provided for multispectral sensors to retrieve the water vapour and aerosol amount based on the input image. For the WV-3 satellite data, the retrieval of water vapour is not applicable due to the absence of the bands in water absorption features, and thus the standard water vapour amount is used. Regarding the aerosol retrieval, the combined VNIR and SWIR WV-3 image allowed to perform aerosol retrieval function using the bands at 660nm and 2165nm (Table 5). Another important option in this settings is to input spectral response function (SRF) for unknown or user-defined multispectral sensors (Harris Geospatial Solutions, 2018a). It is important to use the latest and correct SRF provided by data suppliers. The ENVI provided SRF for WV-3 was the same as the DigitalGlobe's SRF provided in the latest technical note.

Table 5. The input parameters used in FLAASH for the WV-3 September image. Three aerosol models were tested.

Scene and sensor parameters	
Sensor Type	WorldView-3
Sensor altitude (km)	617
Scene center location	36°51'18.73"N; 2°2'13.2"W
Flight date	12-Sep-2017
Flight time (GMT)	11:37:04
Pixel size (m)	7.5
Ground elevation (km)	0.15
Atmospheric parameters	
Atmospheric model	Mid-Latitude Summer
Aerosol model	Maritime/rural/urban
Initial Visibility (km)	40
Multispectral settings	
KT upper channel	SWIR-5 (2165)
KT lower channel	Red (660.1)
Max.upper.chan.reflectance	0.08
Reflectance ratio	0.5

2.2.3. Image processing in FLAASH

After entering all the required input parameters, FLAASH was run for three different aerosol models separately (see Table 5).

2.3. ATCOR – Atmospheric Topographic Correction

The ATCOR software series perform atmospheric and topographic corrections for satellite and airborne sensors in both optical (0.4-2.5µm) and thermal regions (8.0-14.0µm). Three different ATCOR modules are available: ATCOR2, ATCOR3, and ATCOR4. The first mentioned two modules are designed for satellite imagery and the ATCOR-4 is for airborne imagery (Richter & Schläpfer, 2018). In this research, the two satellite versions of ATCOR were used: ATCOR2 (for flat terrain) and ATCOR3 (for rugged

terrain). ATCOR2 is limited to the flat terrain, while ATCOR3 requires an elevation data to process for both flat and rugged terrain. The ATCOR uses look-up tables calculated with MODTRAN-5 radiative transfer code and has separate codes for flat and rugged terrain. For ATCOR, a key formula to perform atmospheric correction is below (Richter & Schläpfer, 2018):

$$L = L_{path} + L_{reflected} = L_{path} + \tau\rho E_g/\pi = c_0 + c_1 DN \qquad (2)$$

L_{path} is the path radiance or photons scattered from atmosphere without having ground contact, τ is the atmospheric transmittance, ρ is the surface reflectance, and E_g is global flux on the ground. From equation (2) the surface reflectance will be:

$$\rho = \frac{\pi\{d^2(c_0+c_1 DN)-L_{path}\}}{\tau E_g} \qquad (3)$$

Where d^2 is the sun to earth distance (d is in astronomic units). The lookup tables for path radiance and global flux are calculated for d=1 in ATCOR. Thus, for ATCOR algorithm, it is important to know the correct calibration coefficients c_0 and c_1 in each spectral band for the specified sensor, and it is required to perform a radiometric calibration before running the algorithm.

2.3.1. Data preparation for ATCOR

Image data preparation
ATCOR uses image data in a unit of [μW/ (cm² * sr * nm)] radiance. The software has some supported sensors with automatic metadata import, and WV-3 is in the list of these sensors. ATCOR reads WV-3 metadata file-.IMD and creates automatically the calibration file- *.cal (Richter, 2018) using 'Read Sensor Meta Data' tool or using the 'Import' tool that reads the TIFF file. The calibration file contains radiometric calibration parameters c_0- offset and c_1- gain per band. For WV-3, these parameters are calculated using the below equations:

$c_0 = 0$; $c_1 = 0.1*absCalFactor / FWHM$

Where absCalFactor is specified in the metadata file (*.IMD); FWHM - is the effective bandwidth ('' effectiveBandwidth'' in μm) as specified in the metadata file. When ATCOR uses data without automatic metadata import, a template *.cal file is used for the selected sensor. In this case, the calibration file needs to be edited manually, because the absCalFactor of the image can be different from the template (Richter, 2018). Thus, the VNIR and SWIR images of WV-3 were processed separately using the automatic metadata import function.

Elevation data preparation
For the ATCOR2 module, the elevation data is accounted as an average value of the scene elevation. The ATCOR3 for rugged terrain uses elevation data as DEM. The DEM file needs to be resized to match the image data and should be in the same coordinate system as the input image. For Rodalquilar, the Digital Terrain Model – MDT05 with 5 m mesh pitch was used for elevation data that was downloaded from the Spanish National Geographic Information Centre (CNIG). The coordinate system of the MDT05 data was converted from ETRS 1989 UTM 30N (EPSG=25830) to the WGS84 UTM 30N (EPSG=32630) to match with the WV-3 satellite images.

2.3.2. Input parameters required for ATCOR

After loading the prepared radiance image data for input, the scene and sensor information are filled automatically from the metadata of the image. Table 6 shows all the required information about the sensor and image acquisition. The atmospheric model in terms of water vapour category was selected as 'Mid-

latitude Summer' according to the geographic location of the area and the image acquisition season-September. Another required atmospheric input parameter is an aerosol type which describes the absorption and scattering properties of particles in the atmosphere. ATCOR provides four different aerosol models namely rural, maritime, urban and desert and first three models were tried in order to select an appropriate model for the study area. The visibility was set to 40km as the days were cloud free and clear skies, but also to make it similar to a previously run FLAASH method (Table 5). The input parameters used for running ATCOR method are summarised in Table 6 below.

Table 6. The input parameters used in ATCOR for the WV-3 image of September. Three aerosol types were tested.

Sensor and scene parameters	VNIR	SWIR
Selected Sensor	wv3_vnir 8ch	wv3_swir 8ch
Sensor incidence angle	28°	28°
Satellite azimuth angle	281°	282.4°
Pixel size	1.2m	7.5m
Solar zenith angle	33.3°	
Solar azimuth angle	167.5°	
Calibration file	Created by automatic metadata import	
Ground elevation	0.15km for ATCOR2 / DEM for ATCOR3	
Atmospheric parameters		
Water vapour category	Mid-latitude summer	
Aerosol type	rural/maritime/urban	
Visibility	40km	

2.3.3. Image processing in ATCOR

Two different modules of ATCOR were tested: ATCOR2-standard sensors for flat terrain and ATCOR3-standard sensors for rugged terrain to see how significant the influence is if there is no elevation data is available. Before processing the image, the SPECTRA module in ATCOR was used to check the expected quality of the reflectance image and to compare the image spectra with reference spectra. This function can be used as a function of estimating the aerosol type and visibility.

2.4. Comparisons of atmospheric correction results

2.4.1. Qualitative visual comparison of reflectance spectra

According to Ben-Dor et al. (2004), evaluation of atmospheric correction method's capability to recover surface reflectance is commonly performed on a qualitative basis, rather than quantitative, using the visual comparison of corrected image and field data on limited target areas. To link and validate corrected image data with field measurements, field sampling sites need to be large enough to cover several pixels in the image (the larger the site, the more pixels can be averaged to reduce noise levels) and spatially uniform, or spectrally 'bland' areas (Clark et al., 2002).

As described in the section above, three sampling sites were measured by a field spectrometer on the ground and spectra collected from each site were averaged and resampled to WV-3 spectral bands. In order to compare these field spectra with image reflectance spectra, I drew regions of interest (ROIs) (Figure 3) covering the same area as was measured with a field spectrometer. For the Wp333 and Wp311 sites (see Figure 3), polygon ROIs were drawn covering 18 and 17 pixels (7.5m pixel size) respectively. For the Wp313-314, there was drawn a line ROI covering 20 pixels. Once the WV-3 radiance images were corrected by using ATCOR and FLAASH, the mean spectra were extracted from the statistics of ROIs

overlaid on each corrected image. Finally, the extracted image spectra from the outcomes of both atmospheric correction methods were directly compared and plotted together with field resampled to WV-3 spectra for visual comparison. The results of the two AC methods have been compared individually within each method with different aerosol types, as well as between two methods with the same aerosol type.

For investigating the consistency of the acquired results and the influences of scene differences, a second WV-3 dataset acquired on 28 May 2017, was processed using ATCOR3 and FLAASH methods. the results were compared with the September WV-3 images on the three reference sites. However, a visual inspection of two images of the different dates showed a difference in geolocation. After plotting and examining GPS waypoints taken during field spectral measurements (Usman, 2018) in both images, the May image showed closer locations to the GPS points. The September image had a horizontal offset. Therefore, based on the May scene, the September image was geo-corrected using two different methods: 1) an image-to-image registration with 25 GCP points and 2) a simple pixel shifting in the header file of the image.

Image registration result showed an overall RMSE of 2.1m which was less than 3.5m CE90 (circular error 90 at 90th percentile) for WV-3. CE90 shows that 90% of the object points have a horizontal error less than the provided value (Barazzetti et al., 2016). Although image-to-image registration RMSE was within the approved limit, it was decided to use a simple pixel shift because the image pixel values will not be changed as occurs in the image-to-image registration process. Hence, to compare the same area on the ground in both scenes, the September image was shifted by 1 pixel (7.5m) to the west (x-axis) based on the ground control points and the May scene.

DigitalGlobe (DG) provides a reflectance image namely AComp to end-users that is corrected atmospherically using Atmospheric Compensation (AComp) algorithm developed by DG. We added the AComp images to the comparison analyses to see their similarity with the field spectral measurements. The WV-3 AComp images of the same dates of May and September 2017, were provided together with radiance images by DigitalGlobe (see Table 1). The AComp algorithm minimizes the effects of haze and atmospheric scattering and absorption by providing an accurate estimate of the aerosol and water vapour amount (DigitalGlobe, 2016). The WV-3 satellite also includes additional CAVIS bands with a 30m resolution that used for atmospheric compensation.

2.4.2. Quantitative comparison and analysis

Apart from the visual and qualitative comparisons of absolute reflectance values, we did a quantitative spectral similarity comparison between the image and the field spectra. For the comparison, we used the Spectral Analyst tool in ENVI software. This tool uses SAM- Spectral Angle Mapper and SFF- Spectral Feature Fitting methods to score the match of a target spectrum to a reference spectrum (Harris Geospatial Solutions, 2018b). In SAM method, the target reflectance spectra (the image spectra) are compared to the reference spectra (the corresponding field spectra) looking for angular similarity between the two spectra (Asadzadeh et al., 2016). The spectra with a lowest angular difference with reference spectra gain the highest score, thus indicating the closest match. The method SFF is an absorption feature-based method which compares the image spectra with reference spectra to fit using a least-square technique (Harris Geospatial Solutions, 2018b).

2.5. Mineral mapping

To investigate influences of different atmospheric correction methods on the mineral map, the satellite images were analyzed by using two different mineral mapping techniques to extract alteration minerals in Rodalquilar. The satellite images used in this analysis were the FLAASH corrected images and AComp

images of May and September scenes. The techniques used for mineral mapping are two different sets of band ratios and a classification using the SAM algorithm.

2.5.1. Band ratio techniques

Band arithmetic is the most commonly used and easy to apply an image processing method for detecting mineral absorption features using basic math operations (Asadzadeh et al., 2016). Band ratio or relative band depth methods use reflectance difference between absorption and shoulder bands and try to minimise reflectance variations associated with topographic slope and albedo differences (Crowley et al., 1989).

In this research, two different band calculation algorithms were used, one for WV-3 bands developed by Sun et al. (2017), and the other one for ASTER bands defined by Rowan (Aleks & Oliver, 2004). From several mineral indices developed for WV-3, the three indices were selected: kaolinite, Al-OH, and calcite (Table 7). They were chosen aiming to map alteration minerals such as kaolinite, alunite, pyrophyllite, illite, and smectite which are well exposed in the study area. The calcite index was applied targeting to map the limestone/sandstone lithological unit (see Figure 2-geological map of the area). On the other hand, the three ASTER band ratios (relative band depth) were selected based on the targeting mineral groups and similarity of WV-3 SWIR bands: 1) alunite/kaolinite/pyrophyllite, 2) sericite/illite/smectite, and 3) dolomite. The ratios were adapted from the ASTER bands and applied to the corresponding similar WV-3 SWIR bands (see Table 7). Table 7 summarises the WV-3 and the ASTER bands in the SWIR region and used band ratio algorithms. The resulting band ratio images and mineral index maps were compared visually and the correlation between FLAASH and AComp outcomes were analysed using scatterplots.

Table 7. WorldView-3 and ASTER bands and selected mineral indices and band ratios by Sun et al. and Rowan respectively.

WV-3 SWIR bands & wavelength region (nm)		ASTER SWIR bands & wavelength region (nm)	
S1	1195 - 1225	-	
S2	1550 - 1590	-	
S3	1640 - 1680	4	1600-1700
S4	1710 - 1750	-	
S5	2145 - 2185	5	2145-2185
S6	2185 - 2225	6	2185-2225
S7	2235 - 2285	7	2235-2285
S8	2295 - 2365	8	2295-2365
-		9	2360-2430
Sun's mineral indices			
Kaolinite	(S3/S5)*(S8/S6)		
Al-OH	(S3/S6)*(S7/S8)		
Calcite	(S6/S8)*(S6/S5)		
Rowan's band ratios			
Alun/kaol/pyr	(S3+S6)/S5	(4+6)/5	
Ser/illite/smec	(S5+S7)/S6	(5+7)/6	
Dolomite	(S6+S8)/S7	(6+8)/7	

Before applying band ratios, the May and September FLAASH corrected, and AComp images have been subset to cover the same extent for further comparisons of the resulting images. Also, the pixels with

values less than zero (produced from FLAASH) and coastal areas under water were masked out to avoid having extremely high or low values.

The Normalized Difference Vegetation Index (NDVI) was calculated for all of the four images to detect vegetated areas and consequently, to suppress the vegetation effect on mineral maps that will be produced later. Hence, vegetation masks were created based on the analysis done by Usman (2018) for the same dataset with a threshold range of 0-0.4. The image pixels with NDVI values less than 0 and greater than 0.4 were masked out in all datasets.

2.5.2.   Mineral mapping using SAM

SAM- Spectral Angle Mapper algorithm was used to analyse the AComp and the FLAASH corrected WV-3 images for mapping hydrothermal alteration minerals exposed in Rodalquilar. The algorithm determines the spectral similarity between image and reference spectra by calculating their angle difference of each reference spectrum versus each image pixel spectrum. Moreover, this value in radians is assigned to the output SAM image pixels (Kruse et al., 1993).

The SAM algorithm was applied to the WV-3 images using a supervised classification tool in ENVI software that compares the angle between endmember spectrum and each pixel spectrum of an input reflectance image (Harris Geospatial Solutions, 2018b). The endmember spectra were extracted from the statistics of regions of interest (ROI) drawn in the WV-3 images. Since Rodalquilar is a well-studied area, the ROIs were created for known locations of mineralisation of alunite, kaolinite, illite and calcite. To obtain more accurate classification results, the input images were spectrally subset to SWIR bands, in order to only focus on diagnostic absorption features of the selected endmember minerals (Hecker et al., 2008). Then, a threshold value is required to set the maximum acceptable angle (in radians) difference between the endmember and image spectra. In this research, two different thresholds were used for all endmembers uniformly: 0.1 radians and 10% of the rule-image histogram. Finally, the SAM produces two images, one is a classified image and the other is a set of rule images equal to the number of endmembers. The classified image shows the best match to a given endmember for each pixel while the pixel values of the rule images show spectral angle difference from the endmember spectrum for each pixel (Harris Geospatial Solutions, 2018b).

3. RESULTS

3.1. ATCOR and FLAASH corrected images

ATCOR2, ATCOR3, and FLAASH atmospheric correction (AC) methods were applied to the WorldView-3 (WV-3) image with 16 bands in VNIR and SWIR wavelength regions. Three different aerosol models namely rural, maritime, and urban were tested with the purpose of defining the optimal aerosol type for the study area Rodalquilar. Other required input parameters and their selections have been explained in chapter 2.

To compare image reflectance spectra with field spectra, regions of interest (ROI) were created for the sites Wp333, Wp311, and Wp313-314, covering the same area as was measured with a field spectrometer (see sections 1.4.3 and 2.4.1 for details). The mean spectra of the three sites were extracted from the statistics of ROI overlaid on ATCOR and FLAASH corrected images, under different aerosol models (Figure 6).
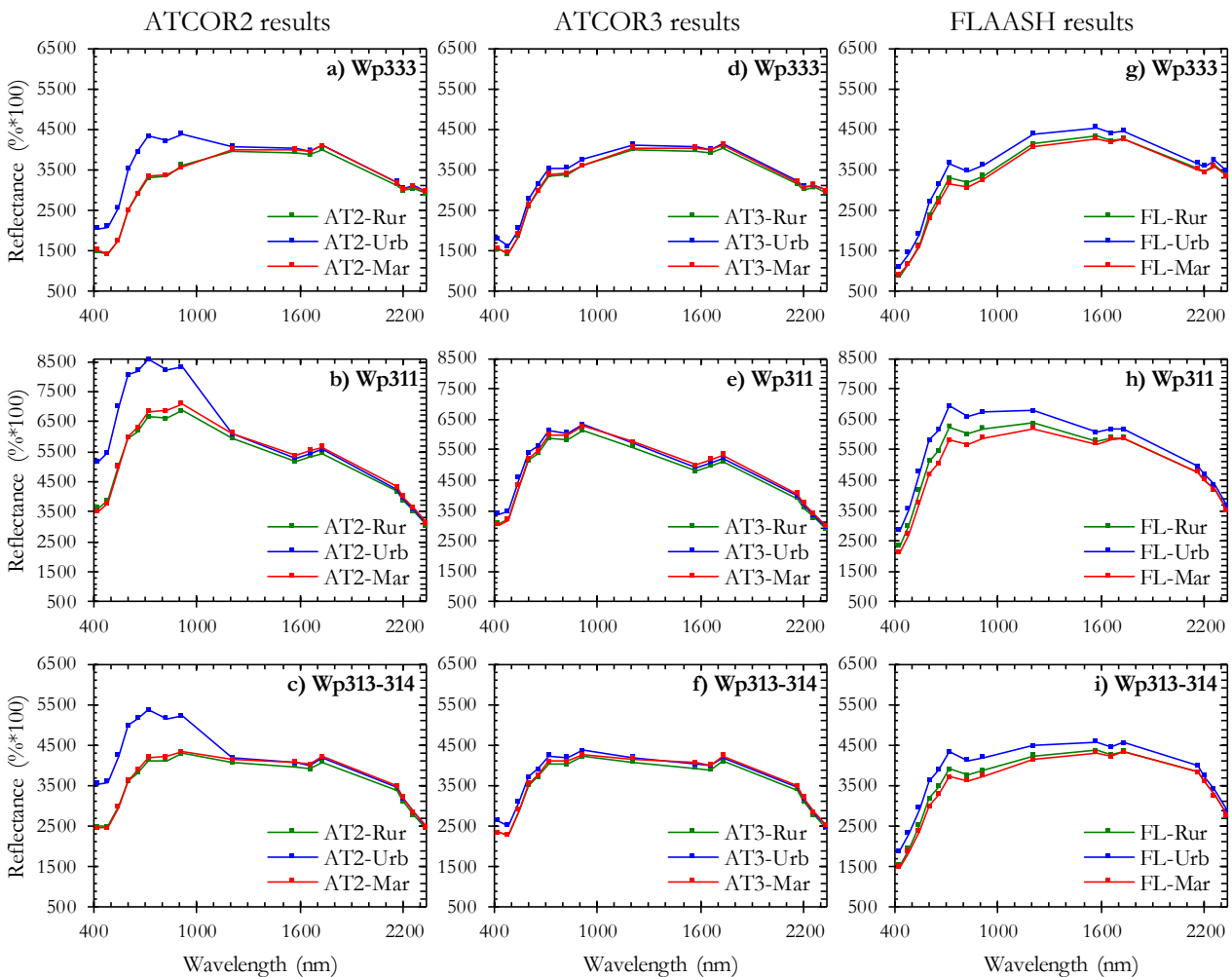
Figure 6. ATCOR2, ATCOR3, and FLAASH corrected image spectra of different sites under varying aerosol models. AT2-ATCOR2 results, AT3-ATCOR3 results, and FL-FLAASH results. Blue lines represent urban aerosol model applied image spectra, green- rural model, and red- maritime respectively.

Two modules of ATCOR methods, one is for flat terrain- ATCOR2 (Figure 6: a-c) and another is for rugged terrain- ATCOR3 with DEM data (Figure 6: d-f), showed overall similar results between different aerosol models for each site except for the urban aerosol model (the blue spectra). The urban aerosol

model of the flat terrain ATCOR2 module produces relatively high reflectance values, greater than 80% in VNIR range compared to the rugged terrain module and their difference is up to 25% for the Wp311 site. The spectral shape differs much in VNIR bands. Thus, for further analysis, only ATCOR3 corrected images (with DEM) were used and compared with the field data.

FLAASH results (the right side of Figure 6: g-i) show more variation for each reference site and each aerosol model. Particularly for Wp311 site, the value difference comprises 11% in the 723nm band. FLAASH tends to estimate higher reflectance in this band than ATCOR results, creating a small spike at 723nm. Its urban aerosol model overall creates higher values than the two other aerosol models in all reference sites. Differences are: 1.2-5.0% in Wp333, 1.3-11% in Wp311, and 1.0-6.2% in Wp313-314.

3.2. Comparison of atmospheric correction results with field data

3.2.1. ATCOR3 results versus field data

The mean reflectance spectra of the three reference sites extracted from ATCOR3 corrected images were directly compared and plotted together with the resampled field spectra (Figure 7).

Regarding the validation site Wp333 (Figure 7a), the image reflectance values in bands 482nm-660nm are well matching with resampled field spectra within the standard deviation limit, while values in NIR and SWIR bands show variations up to 8% difference from the ground data. In terms of spectral shape, image spectra look overall similar with field spectra but with a small tilt up in the VNIR and down in the SWIR bands. Also, some unknown features occur in the image spectra in the 427nm and 1661nm bands of WV-3 image.

For the sandstone/limestone site Wp311 (Figure 7b), the surface reflectance values in the VNIR bands of the image are estimated significantly higher than the ground data with differences up to 16%, and a unknown minimum occurs in the 824nm band that is different from the field data. In contrast, the SWIR bands results are in reasonable conformity with the field data having almost the exact values except for the 1730nm band of the image.

An opposite situation from the Wp311 site is seen for the sandy beach Wp313-314 site (Figure 7c). The reflectance values in the VNIR bands of WV-3 image are well matched with the ground data but with unknown features in the 427nm and 824nm bands. The results in all the SWIR bands are estimated lower than the field reflectance values with an average difference of 8%.
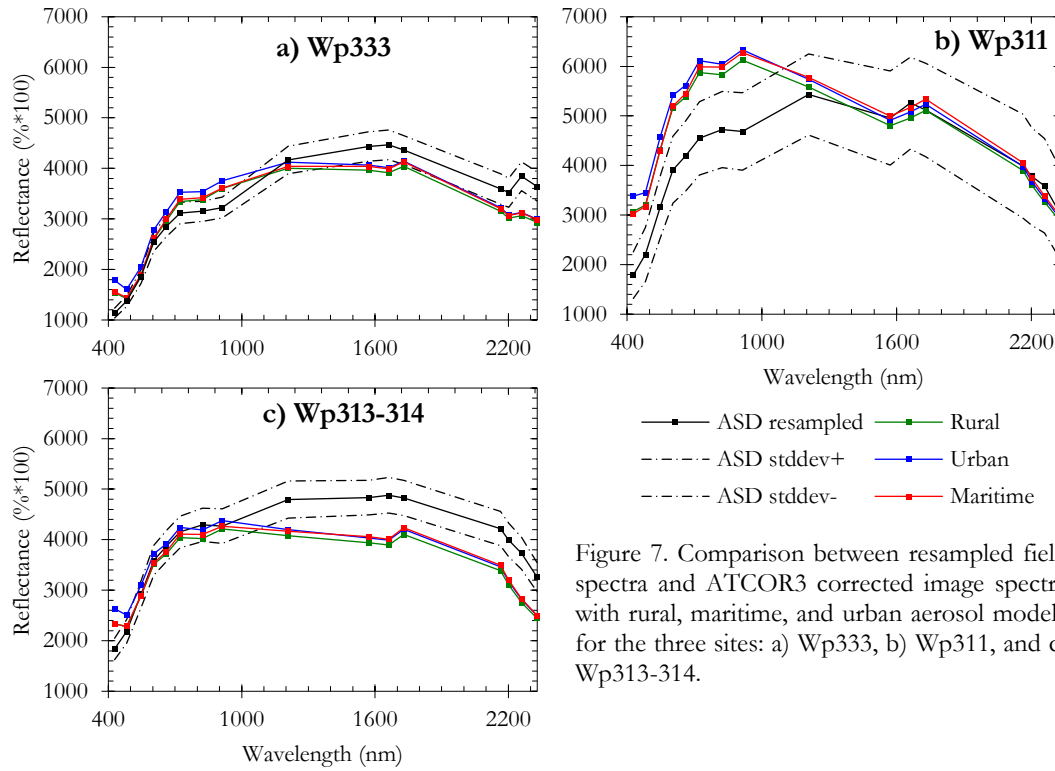
Figure 7. Comparison between resampled field spectra and ATCOR3 corrected image spectra with rural, maritime, and urban aerosol models for the three sites: a) Wp333, b) Wp311, and c) Wp313-314.

In addition to the direct visual comparison of absolute reflectance values, two spectral matching techniques Spectral Angle Mapper (SAM) and Spectral Feature Fitting (SFF) have been used to measure the spectral similarity between the image spectra and resampled field spectra. Results of matching scores are shown in Table 8 below.

The highest scores by SAM method are obtained for the maritime aerosol model results for all three sites indicating the closest match with the field data while the lowest scores correspond to the urban aerosol model results. The highest scores by SFF method correspond to the Wp311 site, and the lowest scores are obtained for the Wp333. The SFF scores of different aerosol models showed almost the same values with a negligible difference of 0.001 within one site.

Table 8. Spectral similarity results between ATCOR3 corrected image spectra and resampled field spectra using SAM & SFF methods.

| Sites: | Wp333 | | Wp311 | | Wp313-314 | |
Methods:	SAM	SFF	SAM	SFF	SAM	SFF
Maritime	0.791	0.913	0.712	0.958	0.794	0.951
Rural	0.783	0.910	0.685	0.957	0.777	0.951
Urban	0.748	0.910	0.658	0.955	0.738	0.949

In general, the maritime aerosol model appeared to be the best model for the three validation sites, and the site Wp333 showed the closest results with field data for ATCOR3 atmospheric correction method.

3.2.2. FLAASH results versus field data

The reference sites spectra extracted from FLAASH corrected images with rural, maritime and urban aerosol models were compared with the resampled field spectra. Figure 8 illustrates the spectral comparison for each validation site.

There is reasonable conformity in shape between field and image spectra. For the Wp333 site, the overall shape of the image spectra is similar to the field spectra within the standard deviation limits except for the urban aerosol model (Figure 8a). The urban aerosol model has the largest difference of 5.5% in the 723nm band of the image for this site. Besides, an unknown minimum occurs at the 1661nm band (SWIR3 band), while it is not present in the field spectra.

Regarding the site-Wp311(sandstone and limestone exposure), the image reflectance spectra are always higher than the field spectra for all three aerosol model results (Figure 8b). Particularly, the urban aerosol model showed differences of 10-24% in VNIR bands and 6-13% in SWIR bands. Moreover, the difference in the results of the three aerosol models has more variation compared to the other two sites.
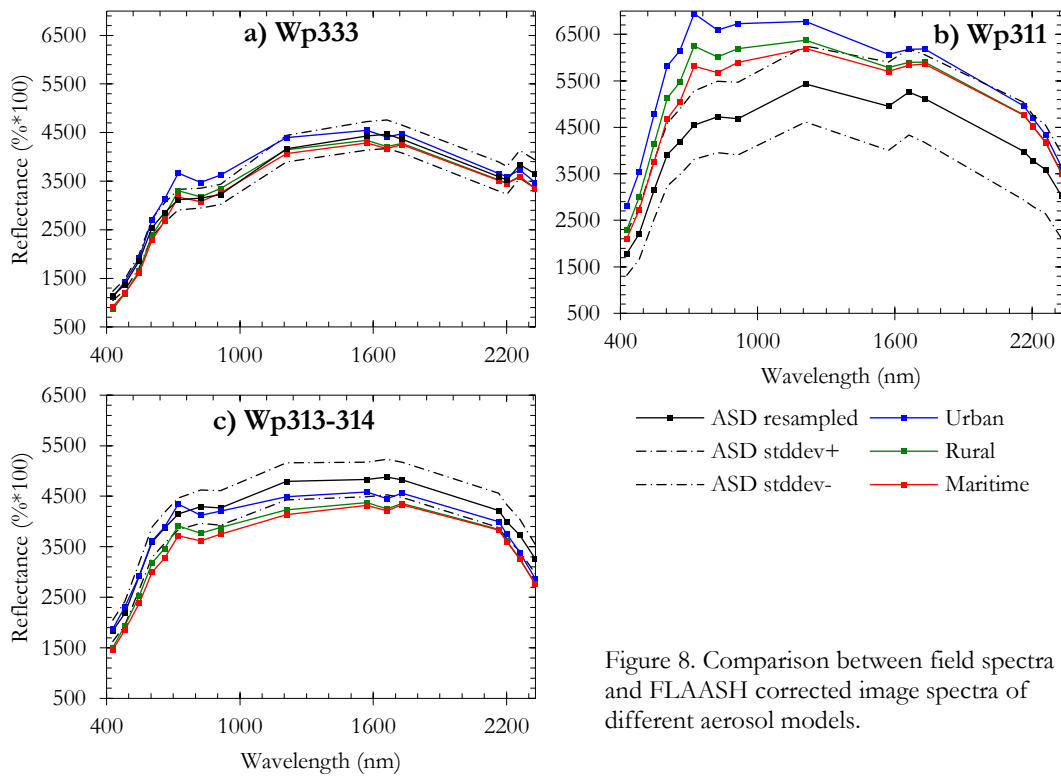
Figure 8. Comparison between field spectra and FLAASH corrected image spectra of different aerosol models.

The image spectra of the sandy beach site Wp313-314 show a good overall similarity in spectral shape with the field resampled spectra (Figure 8c). In contrast to the Wp311, the reflectance level was lower than the field data except for the urban aerosol model. The rural and maritime aerosol models' results are lower than the standard deviation limit. The largest difference of 6.7% is seen in the 824nm band of the image in the maritime aerosol model results.

The FLAASH corrected image spectra were then compared with resampled field spectra using two spectral matching techniques SAM and SFF (Table 9). From the SAM, the maritime aerosol model's results get the highest scores in two sites Wp333 and Wp311 except for Wp313-314, whereas the urban aerosol model's results obtain the lowest scores in all three sites indicating the worst match with the field spectra. Overall, the Wp313-314 site gets the highest scores in all three aerosol models while the image reflectance levels are always lower than the field mean spectrum. From the SFF, differences between aerosol models were negligible (up to 0.004) within the same site.

Table 9. Spectral similarity results between FLAASH corrected image spectra and resampled field spectra using SAM & SFF methods.

Sites:	Wp333		Wp311		Wp313-314	
Methods:	SAM	SFF	SAM	SFF	SAM	SFF
Maritime	<u>0.926</u>	<u>0.967</u>	<u>0.920</u>	<u>0.974</u>	0.939	<u>0.967</u>
Rural	0.912	0.966	0.868	0.974	<u>0.947</u>	0.965
Urban	0.891	0.966	0.801	0.972	0.911	0.963

3.2.3. Comparison between ATCOR3, FLAASH, and field data

In the previous sections, outcomes of ATCOR and FLAASH atmospheric correction (AC) methods have been compared separately with the field resampled spectra. As it was shown previously that maritime aerosol model appeared to be the optimal aerosol model for both methods, only the results of this model were used for comparison between the two methods.

Figure 9 displays comparative plots of the resampled field spectra and the image spectra corrected by ATCOR3 and FLAASH with the maritime aerosol model for each of three validation sites. Visually, the overall shape of the FLAASH corrected image spectra are more similar to the field spectra than ATCOR3 results. The ATCOR3 corrected image spectra look to be tilted such that it is lifted in VNIR region and lowered in SWIR region.
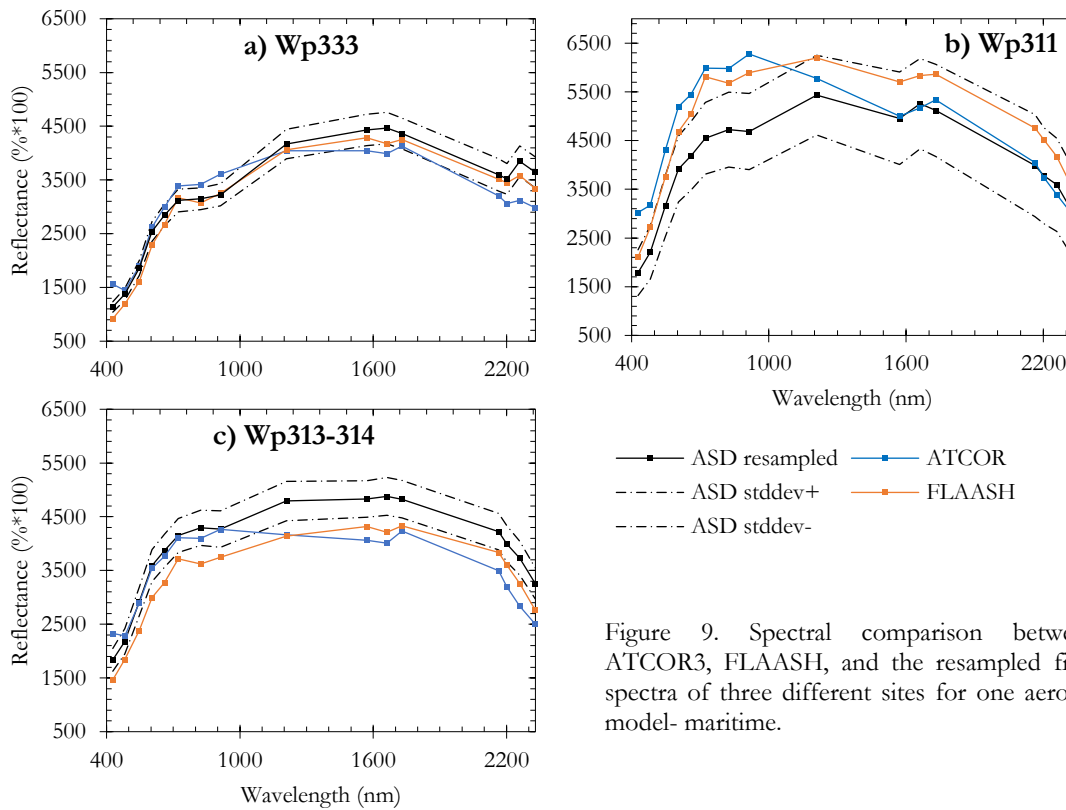
Figure 9. Spectral comparison between ATCOR3, FLAASH, and the resampled field spectra of three different sites for one aerosol model- maritime.

In terms of absolute reflectance differences, the ATCOR3 produces results closer to the field data in 482nm-660nm bands of the image compared to the FLAASH, having differences of 0.3-1.5% for the two sites Wp333 and Wp313-314 (Figure 10). For the Wp311 site, ATCOR3 results show differences up to 16% from the field data in VNIR bands of the image (Figure 9and Figure 10). In ATCOR3, reflectance

values in the first 427nm band are always higher than the adjacent 482nm band while the field spectra and FLAASH results show an opposite trend.
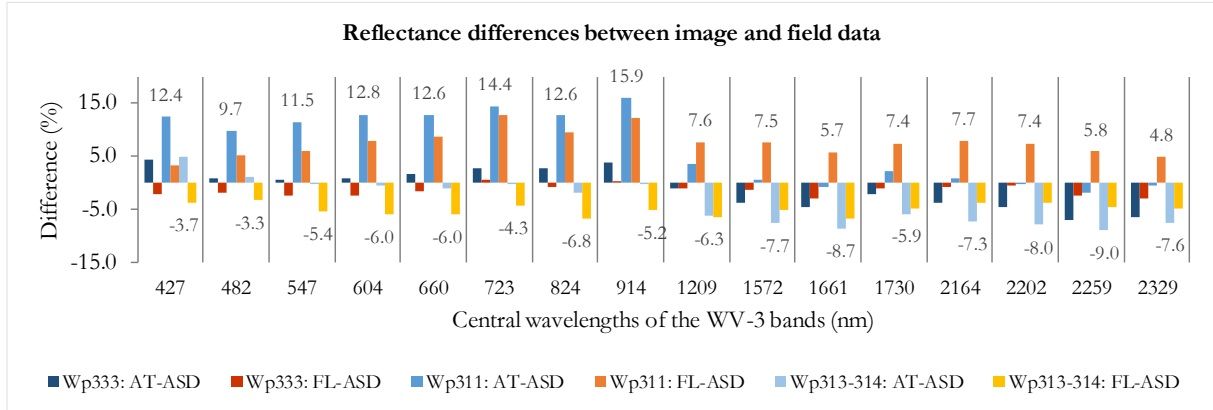
Figure 10. Differences of the surface reflectance estimated by ATCOR3 (AT) and FLAASH (FL) and measured in the field (ASD- resampled to WV-3 bands) of three reference sites. Positive values show overestimation and negative values show underestimation of the reflectance compared to the field data. The highest positive and negative values are labelled.

Regarding the FLAASH estimated reflectance, deviation of the differences from the field data is relatively constant in all bands, and this makes the spectra to look more similar to the resampled field spectra (Figure 9 and Figure 10- red to yellowish bars). For the Wp333 site, where the field spectra were collected concurrently with the WV-3 image acquisition time, FLAASH gave the closest results to the field data compared with the two other sites (Figure 9a and Figure 10-red bars).

For ease of comparison, the previously presented SAM and SFF spectral similarity results for ATCOR3 and FLAASH maritime aerosol model are combined in Table 10. By SAM method, the ATCOR3 corrected image spectra scored lower than the FLAASH outcomes in all sites showing that there are greater angle differences from the resampled field spectra.

Based on the visual and direct comparisons of absolute values and spectral matching results, the FLAASH atmospheric correction method appears to show results closer to the field data than ATCOR3 method for all three sites.

Table 10. Results of spectral similarity comparisons of FLAASH and ATCOR3 outcomes (the maritime aerosol model).

Sites	Wp333		Wp311		Wp313-314	
Methods	ATCOR3	FLAASH	ATCOR3	FLAASH	ATCOR3	FLAASH
SAM	0.791	0.926	0.712	0.920	0.794	0.939
SFF	0.913	0.967	0.958	0.974	0.951	0.967

3.2.4. Comparison of May and September WV-3 scenes

To investigate the consistency of the acquired results and the influences of scene differences, a second WV-3 dataset, acquired on 28 May 2017, was processed using both ATCOR3 and FLAASH methods. Detailed input parameters of May scene for AC methods are presented in Appendix 1. Figure 11 shows the spectral comparison between May and September images on three reference sites for both ATCOR3 and FLAASH methods with maritime aerosol model applied.
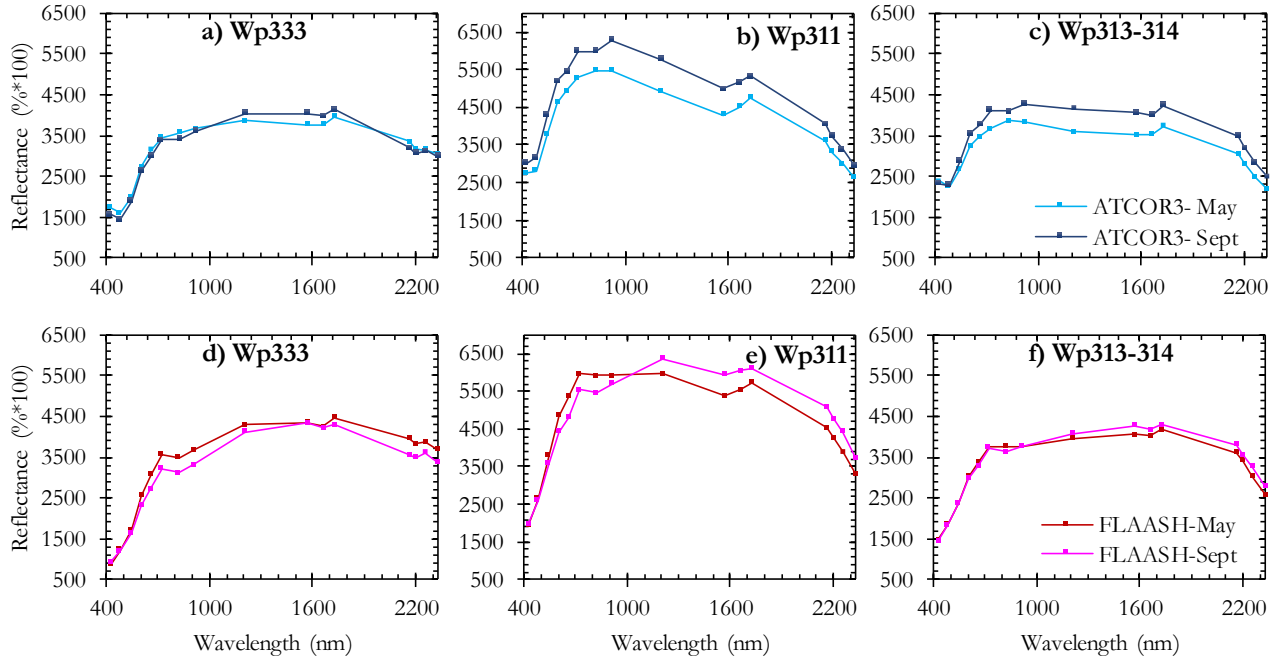
Figure 11. Spectral comparison between May and September WV-3 images corrected by ATCOR3 and FLAASH AC methods on three reference sites. The upper row shows comparisons of ATCOR3 results and the lower row shows comparison plots of the FLAASH results for each site.

For ATCOR3 results, overall spectral shapes look similar, but brightness difference is significant for Wp311 (2.8-8.6% in all bands) and Wp313-314 (0.4-5.5% in all bands) sites. A small unknown feature observed in September image at 824nm is not seen in May image for all three sites (Figure 11a-c).

Regarding the FLAASH outcomes, the Wp311 site has the largest difference in reflectance values (5.7% in the 1571nm band of WV-3), while the Wp313-314 site has the closest values with differences of 0.06-2.2% in all bands between two scenes. This large difference of the Wp311 site might be related to the inhomogeneity of the area and also mismatching between the area measured in the field and drawn region of interest (ROI) on the image.

3.2.5. Comparison between FLAASH, AComp and field data

Furthermore, the WV-3 AComp images from the same May and September 2017 acquisitions, were used for comparison, as they are reflectance images delivered to end-users by the data supplier. From the previous comparison results, FLAASH corrected images appeared to have less differences than ATCOR3 results. Therefore, comparisons were done between AComp, FLAASH results and the field data for September image; and for May image, only between AComp and FLAASH outcomes due to an absence of in-situ data. The spectral comparisons are shown in Figure 12.

For May acquisition (Figure 12a-c), the average difference between FLAASH and AComp were 1.5%, 5%, and 2% for Wp333, Wp311, and Wp313-314 sites respectively. The maximum difference of 10% is

observed at 660nm for the Wp311 site (Figure 12b). The AComp results in the last 2329nm band are higher than FLAASH with differences of 3-5% for all three sites (Figure 12 top row & green spectra). Particularly, for the Wp333 site, the reflectance is estimated even higher than the previous 2259nm band (Figure 12a). On the other hand, the FLAASH appeared to estimate higher values in the 723nm band of the image for all three sites compared with AComp, having the largest difference of 10% for the Wp311 site (see Figure 12b upper left corner).

For the WV-3 September image, all the above-mentioned differences are present as well. Both AComp and FLAASH methods produced higher values in the 1730nm band than the adjacent 1661nm band of the image, showing a little peak in the spectral shape where the resampled field spectra show a small absorption dip instead.
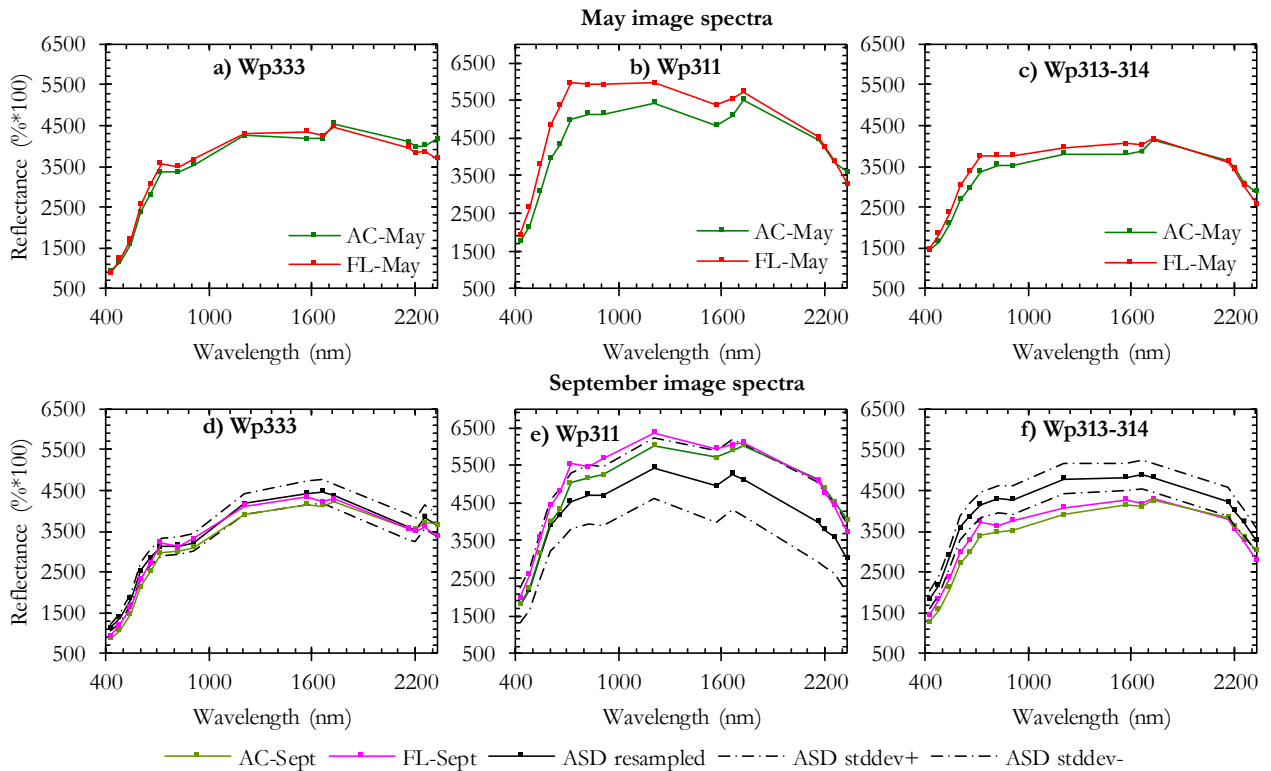
Figure 12. Spectral comparison of AComp (AC) and FLAASH (FL) corrected WV-3 images of May and September acquisitions for each reference site. September image spectra compared with resampled field spectra, yet for May image, in-situ data has not been collected.

To summarise, the FLAASH method tends to estimate higher values in the 723nm band of the WV-3 than AComp, whereas the AComp tends to produce relatively higher values in the last 2329nm band from both May and September images for all three reference sites. Similarly, to the previous comparisons, the Wp311 site has the largest differences between AComp and FLAASH results in both May and September images.

3.3. Mineral mapping results

After direct comparisons of reflectance spectra of two scenes and different atmospheric correction (AC) methods, the FLAASH corrected image and AComp reflectance image were analysed using band ratio techniques and SAM mapping method to extract alteration minerals in Rodalquilar. These analysis aims to evaluate differences in mineral maps produced from abovementioned two different reflectance images. The comparisons of the band ratio results were done visually and as scatterplots.

3.3.1. Band ratio results

WorldView-3 mineral indices

Three mineral indices namely Kaolinite, Al-OH, and Calcite developed by Sun et al., (2017) for WV-3 data, were applied to the WV-3 May and September images. The bands used in mineral indices and their wavelengths are provided in Table 7. Kaolinite and Al-OH indices were chosen aiming to map advanced and intermediate argillic alteration zones that contain alteration minerals such as kaolinite, alunite, pyrophyllite, illite, and smectite. The Calcite index was applied targeting to map the limestone/sandstone lithological unit (see Figure 2-geological map of the area). Figure 14 shows the image processing results of three mineral indices applied on AComp and FLAASH corrected images and corresponding scatterplots showing their correlations for each mineral index are shown in Figure 13.

The kaolinite index is defined as (S3/S5)*(S8/S6). To compare visually, May image results showed a similar spatial pattern between AComp and FLAASH (Figure 14a-b). From their scatterplot (Figure 13a), it can be seen that the two images are highly correlated (correlation is 0.995), yet the AComp image produces higher values than the FLAASH result. In contrast, the September kaolinite images had a clear visible difference between AComp and FLAASH (see Figure 14c-d). The kaolinite abundances increased significantly in the central part of the AComp image compared with the FLAASH outcome. Here, we observed a striping effect (Figure 14c) and the predicted area of abundant kaolinite is seemed to spatially fall within the same area where the stripping occurs. However, a smaller occurrence of kaolinite in the north-eastern part of the image is mapped relatively similar in both images.

The Al-OH index is defined as (S3/S6)*(S7/S8). From the visual comparison, the May-AComp result (see Figure 14e) differs considerably in spatial pattern compared to the other three images (Figure 14f-h). The scatterplot of this index maps (Figure 13c) shows that the May-AComp results are calculated constantly lower than the FLAASH results. The September Al-OH images showed a lower correlation of 0.981 than May images with more scattered AComp values (Figure 13d).

The Calcite index is defined as (S6/S8)*(S6/S5). Visually, the May-FLAASH result (Figure 14i) showed more abundant calcite than May-AComp, and this can also be seen from their scatterplot shown in Figure 13e. The correlation between them is very high 0.999, but the data values differ significantly. Regarding the September images, the correlation between AComp and FLAASH is high 0.993, and the data range also appears to be similar falling within the 1:1 line. However, the FLAASH results are mostly calculated higher than the AComp (Figure 13f).
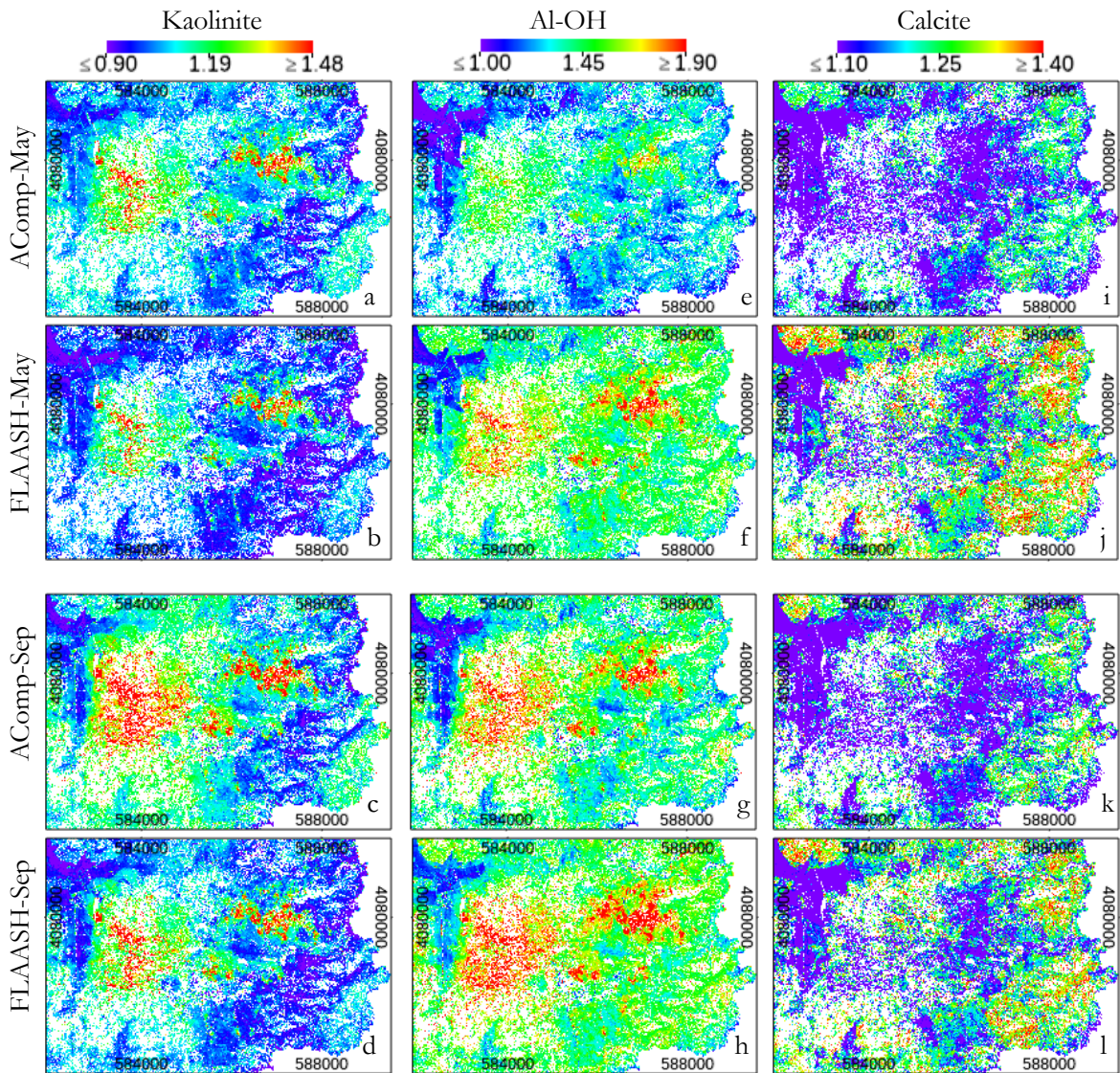
Figure 14. Kaolinite, Al-OH and calcite mineral indices maps produced from AComp and FLAASH corrected WV-3 images. The top two rows show May images and the bottom two rows show September images.

Figure 13. Scatterplots of Sun's mineral indices maps created from AComp and FLAASH reflectance images. The correlations of the images are shown in the upper left corner.

The Rowan's band ratios defined for ASTER bands.

The next method of mapping mineralogy of the study area was band ratios developed for ASTER sensor. The previously used Sun's mineral indices appeared to be influenced much by one specific band of WV-3 image and also, spatial patterns of kaolinite and Al-OH indices were discriminated relatively similar. Therefore, well-established ASTER band ratios developed by Rowan (Aleks & Oliver, 2004) were used and adapted to the WV-3 bands. Table 7 shows the similarity of ASTER and WV-3 bands and Rowan' band ratio formulas. The used three band ratios are:

1. alunite/kaolinite/pyrophyllite: (S3+S6)/S5 or (1661nm+2202nm)/2163nm,
2. sericite/illite/smectite: (S5+S7)/S6 or (2163nm+2259nm)/2202nm,
3. dolomite: (S6+S8)/S7 or (2202nm+2329nm)/2259nm.

Figure 16 shows the results of band ratios and Figure 15 shows scatterplots of these results. The alunite/kaolinite/pyrophyllite ratio images showed similar overall patterns in all images but appeared to be more abundant in September images (Figure 16a-d). Though, the correlation between AComp and FLAASH September images was 0.977 the lowest among all images (Figure 15b). This might be due to striping in September AComp image. The sericite/illite/smectite ratio images are all spatially very comparable and have the highest correlation between the datasets (Figure 15e-h - images in the centre). Differences in value ranges were also low. Regarding the dolomite ratio images, data range of May AComp image was the highest and consequently, produced relatively intense map compared to the other results (Figure 15i). This can also be observed from the scatterplot of AComp and FLAASH May images data (Figure 16e). Almost all the data values of the AComp May dolomite image are lower than 1:1 line comparing to the FLAASH results. This result is most likely caused by higher reflectance in the last band of the AComp May image (see section 3.2.5). The dolomite spatial pattern of May and September FLAASH outcomes appeared to be in a good matching contrary to the AComp outcomes.
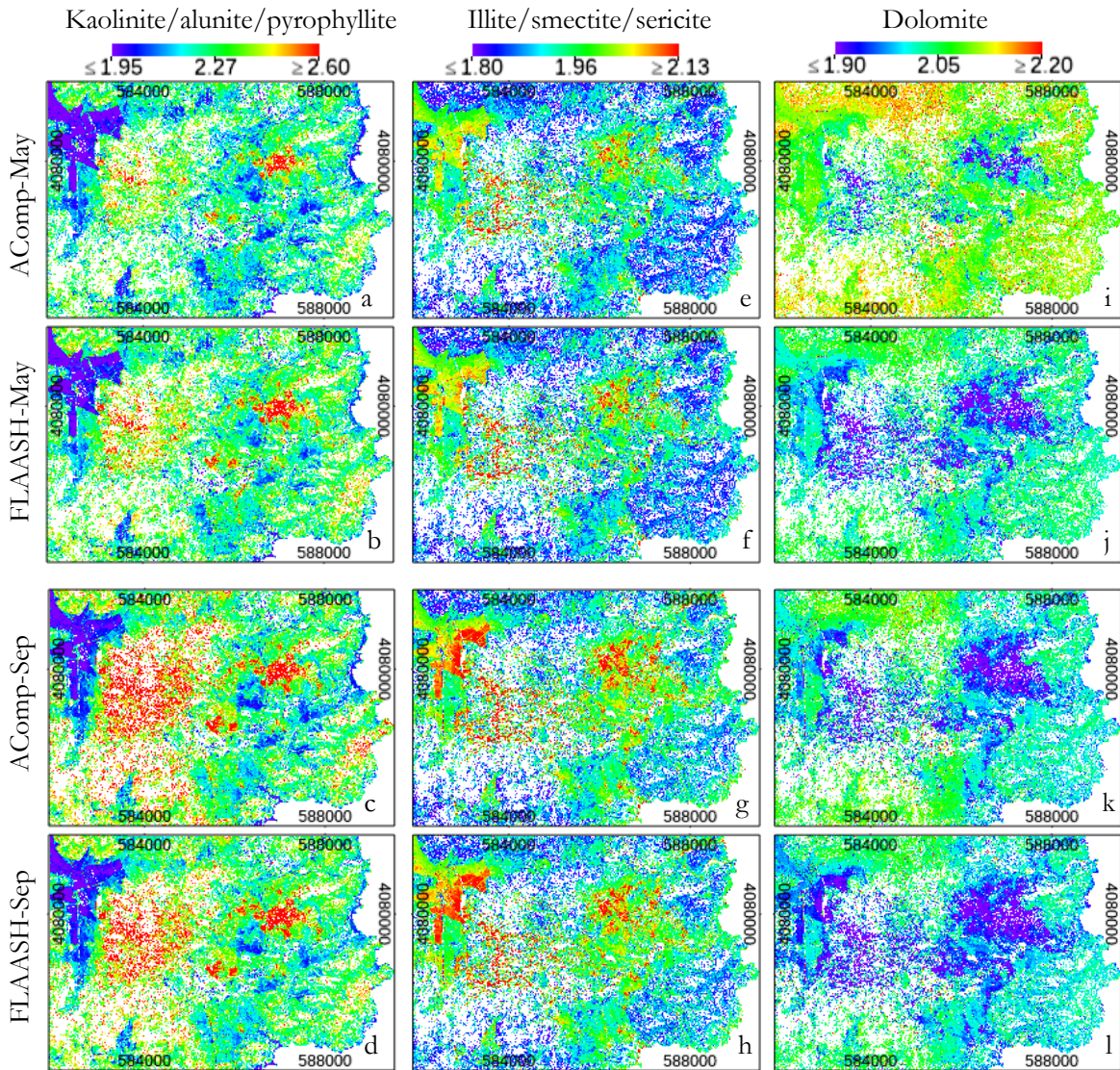
Figure 16. Band ratios defined by Rowan (USGS) for ASTER bands. Kaolinite/alunite/pyrophyllite, illite/smectite/sericite and dolomite ratios produced from AComp and FLAASH corrected WV-3 images. The top two rows show May images and the bottom two rows show September images.

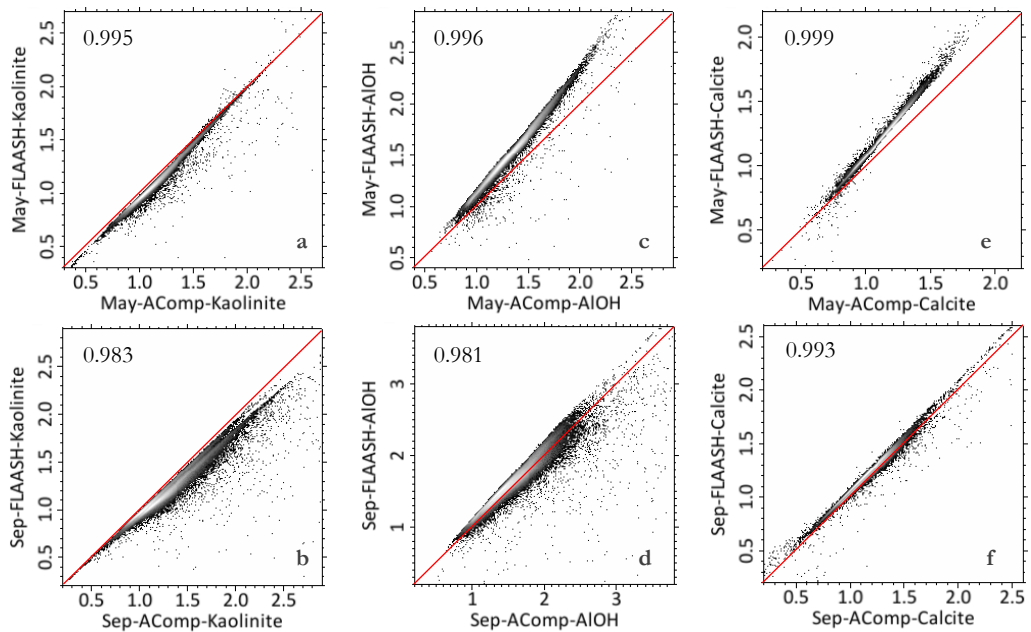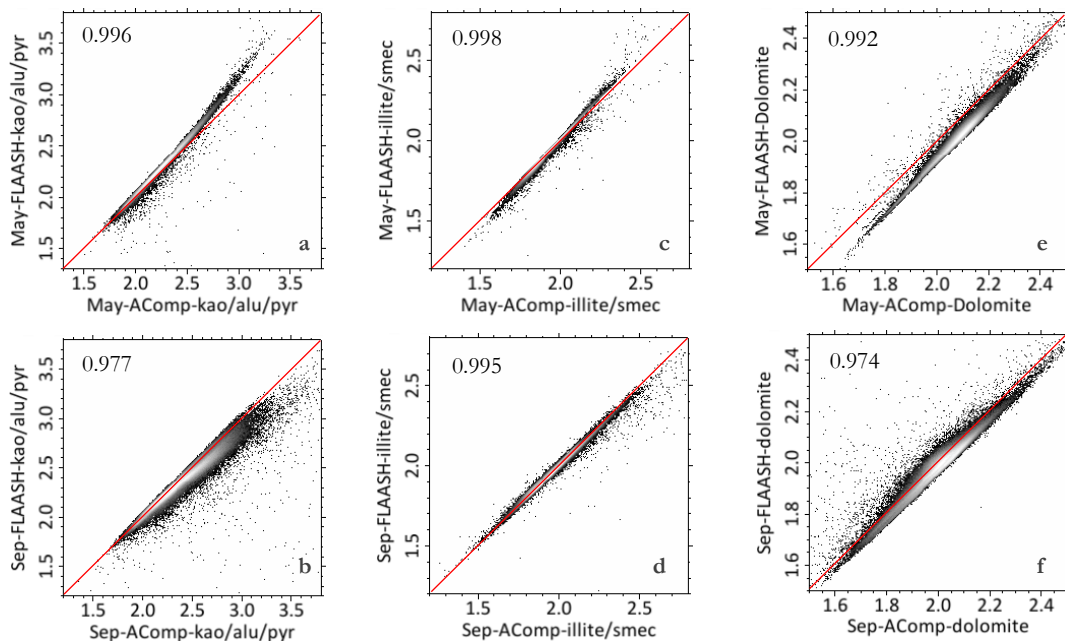Figure 15. Scatterplots of Rowan's band ratios created from AComp and FLAASH reflectance images. The correlations of the images are shown in the upper left corner.

3.3.2. SAM mineral mapping results

After comparing band calculation techniques of mineral mapping, a widely used SAM (Spectral Angle Mapper) was used to analyse AComp reflectance image and FLAASH corrected WV-3 images of May and September scenes. Since Rodalquilar is a well-studied area, regions of interest (ROI) were created for known locations of mineralization of alunite, kaolinite, illite and calcite for extracting endmember spectra.

ROIs were drawn based on image spectral analysis, decorrelation stretched (DS) image of RGB colour composite made of SWIR bands (R=2160nm, G=2205nm, B=2330nm), and previous band ratio results. The DS image shows alunite as cyan due to lower reflectance in R=2160nm (deepest absorption feature). Calcite appears yellow-green because of low reflectance in a 2330nm band where absorption feature occurs. Illite is reddish to magenta due to high reflectance in the 2160nm band while kaolinite is blueish to magenta because of higher values in 2330nm bands and lower reflectance in 2160nm and 2205nm. In this way, ROIs were drawn, and a mean spectrum of each ROI was selected as an endmember spectrum. For each image, a separate endmember collection was used for the classification, but the endmember spectra were collected from the same locations on the image. Locations of ROIs and their mean spectra are shown in Figure 17.
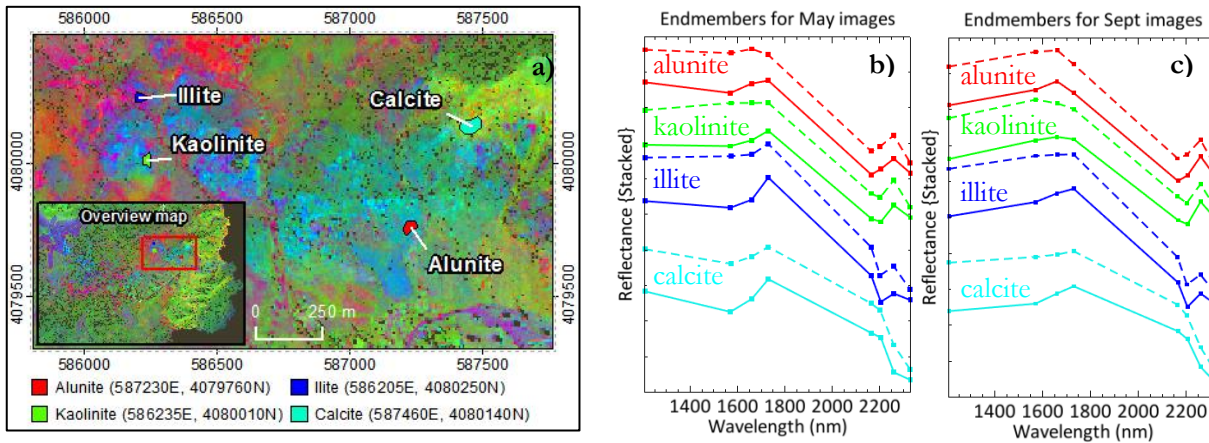
Figure 17. a) Location map of ROIs used for endmembers and their coordinates of the centre point overlaid on DS image. b) Endmember spectra for May images, c) Endmember spectra for September images. Solid lines are AComp image spectra and dashed- FLAASH image spectra.

For the SAM classification method, a single threshold value of 0.1 radians was used for all endmembers uniformly. This is the maximum acceptable angle between the endmember spectrum and the image pixel spectrum. Before running SAM classification, the input images were spectrally subset to SWIR bands, in order to consider only diagnostic absorption wavelengths of the minerals in endmember collection. SAM classification results analysed from AComp and FLAASH images are shown in Figure 18.

Visual comparison of the mineral maps shows that spatial patterns of the identified minerals appear to be similar between the outcomes from May-AComp and May-FLAASH corrected images with differences of alunite abundances (7% in May-AComp and 3.8% in May-FLAASH) in the south-eastern and south-northern parts of the area (Figure 18a-b). In contrast, mineral maps produced from September AComp and FLAASH images have a significant difference in illite abundance. The abundant illite in the September-AComp may be caused by the striping effect that was seen in the previous band ratio images as well. Also, it is apparent that calcite is overpredicted in all images covering the whole study area while calcite spatial distribution is only at the eastern part of the study area (see Figure 2 the geologic map). Class distribution statistics of the above presented SAM classified images are compared and shown in Figure 19.
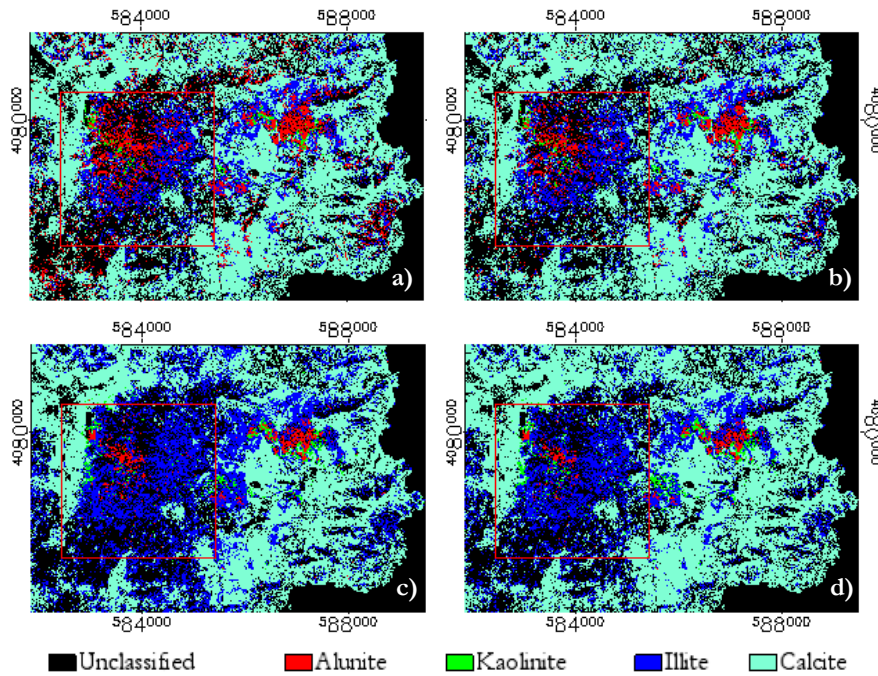
Figure 18. Mineral maps produced from SAM classification method with 0.1rad threshold. a) May-AComp, b) May-FLAASH, c) Sept-AComp, d) Sept-FLAASH.

The percentages of unclassified areas are very close between all four images (39% - 40.3% in Figure 19) because most of the unclassified pixels correspond to the masked areas of vegetation cover (NDVI mask) and water. Their small difference is falling in some agricultural areas located in the north-western part of the images (Figure 18) that are not masked because of low NDVI values (around 0.15). Abundances of alunite, kaolinite and illite are quantified almost equally within the same scene, but they differ considerably between the two different scenes.
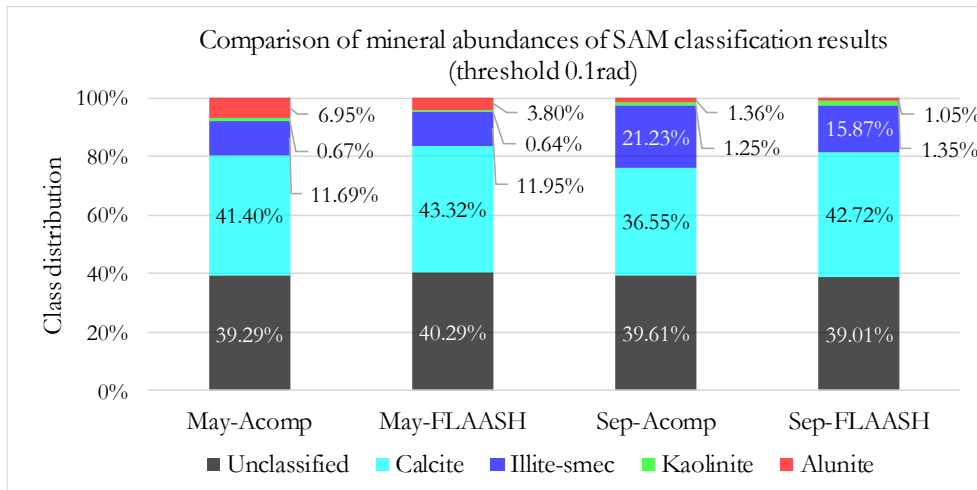
Figure 19. Mineral abundances calculated from SAM classification results for May and September images of AComp and FLAASH outcomes.

Due to the unrealistic classification of calcite abundance, it was decided to change the threshold value and reclassify the images using the rule-images of endmembers. The histogram percentage of 10% was selected for the threshold, based on visual inspection of the spectral plot of the images. The classification results are shown in Figure 20 and their corresponding class distribution statistics are provided in Figure 21.
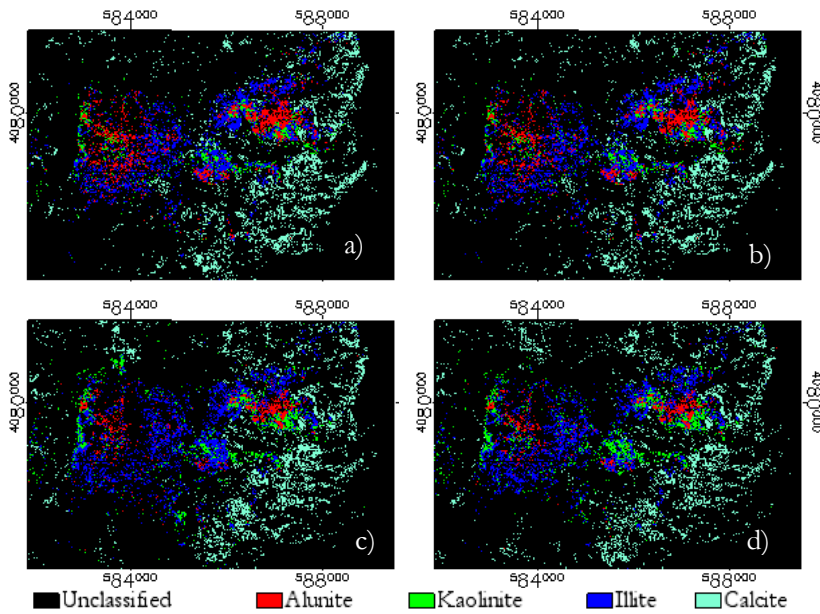
Figure 20. SAM classified images with 10% threshold: a) May-AComp, b) May-FLAASH, c) Sept-AComp, d) Sept-FLAASH.

This classification result with the 10% threshold changed the September images significantly by decreasing illite and calcite abundances (Figure 20c-d). Now, spatial patterns of the mineral distributions look relatively similar in all images, and their percentage quantities appear to be very close between the four images as well (Figure 21). Kaolinite abundance is increased from a range of 0.67-1.35% to the range of 1.53-2.38%; this can be observed clearly in September images (green coloured area in Figure 20c-d).

Based on the above presented two different classification results, it can be concluded that SAM classification results are highly dependent on the selection of the threshold values regardless of different input reflectance images derived from different atmospheric correction methods.
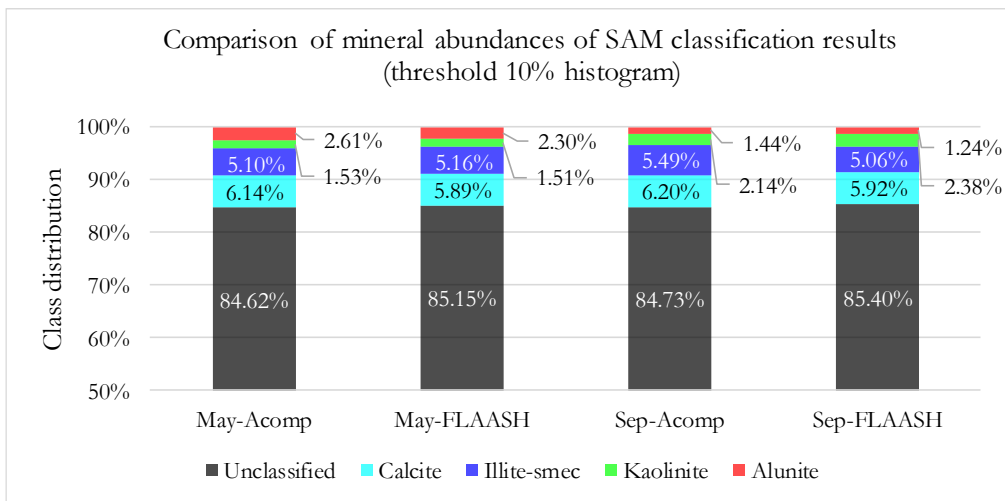
Figure 21. Mineral abundances calculated from SAM rule-image classification results (10% histogram threshold) for May and September images of AComp and FLAASH outcomes.

4.   DISCUSSION

In this research, two different radiative transfer model (RTM) based atmospheric correction (AC) methods ATCOR (two modules ATCOR2 for flat and ATCOR3 for rugged terrains) and FLAASH were applied to WorldView-3 (WV-3) images from two acquisition dates May and September 2017. Each of the AC methods was performed with three different aerosol models aiming to define the optimal aerosol type for the study area. Their results were directly compared with in-situ field measurements. Several comparisons were done: between the three aerosol models, between two AC methods, and between two scenes. Additionally, DigitalGlobe's reflectance image namely AComp images were added to the comparisons. Finally, two methods of image analysis band ratio technique and Spectral Angle Mapper (SAM) were used to process May and September 2017 WV-3 images for mapping alteration mineralogy of Rodalquilar. The following subsections will discuss the results comparisons of AC methods and mineral mapping results, and the side issues faced during the research.

4.1.   Aerosol model differences in ATCOR and FLAASH corrected images

The results of atmospheric corrections applied on September WV-3 image by using ATCOR2 (the flat terrain module), ATCOR3 (the rugged terrain module), and FLAASH methods with selected aerosol models, have been presented as mean spectra of three reference sites (Figure 6).

Generally, the main differences between aerosol models are in the VNIR bands of the WV-3 data. This is the wavelength region where the electromagnetic spectrum is influenced most by aerosol scattering and absorption. ATCOR methods (Figure 6- a-f) tend to produce higher values in the first band of the image at 427.4nm than the FLAASH method. This is also present in other areas selected for verification on the image: grass, bare soil and bright target (see Appendix 2). The ATCOR calculates the surface reflectance differently in the deep blue band than other wavelength regions. It uses an empirical approach that assumes the surface reflectance of the reference dense dark vegetation at 400nm to be 0.6 times the reflectance of the 480nm. The surface reflectance for bands in between is then linearly interpolated (Richter & Schläpfer, 2018). Therefore, the ATCOR tendency of computing higher values in the first 427nm band can be related to this empirical approach.

In our experiments of AC, mostly the urban aerosol model appeared to have the greatest difference compared with rural and maritime aerosol models for all three methods and all reference sites and tended to estimate higher reflectance values than other two aerosol models (Figure 6- blue lines). Especially, ATCOR2 with urban aerosol model produced relatively high reflectance values with differences up to 25% from the field spectra. This high estimation of the surface reflectance is observed in other target areas as well. The reason is most likely related to the compositional differences of the aerosol models. A study about effects of different aerosol types on the surface reflectance done by Tirelli et al. (2015) in the urban-coastal area, showed similar results for urban type aerosols with large differences compared to rural and maritime. The urban type aerosols are modelled as to have more absorbing water-soluble components than the two other aerosol models and leading to overestimation of surface reflectance (Tirelli et al., 2015; Erlick & Frederick, 1998).

ATCOR3 results showed less variations between different aerosol models than two other methods. This might be a result of ATCOR3 algorithm's advantage of using elevation data that computes the surface reflectance of each pixel accounting for the atmospheric path radiance and transmittance functions as elevation dependent: $L_{path}(z)$ and $\tau(z)$ in the equation (3) (Richter, 1997). The aerosol type determines the wavelength behaviour of the path radiance.

4.2. Comparisons of atmospheric correction results with field data

4.2.1. Comparison between ATCOR, FLAASH, and field data

Spectral comparison of ATCOR3 results versus the resampled field spectra was presented in Figure 7. Overall, the reference sites' image spectra look relatively similar with field resampled spectra but with a small tilt such that lifted in VNIR region and lowered in SWIR regions. This tilt may be caused by the use of separate processing for VNIR and SWIR images of WV-3 data (see also section 2.3.1). However, the current research did not focus on further investigations to confirm this assumption.

FLAASH produced the closest results to the field data for the Wp333 site which was measured concurrently with the image acquisition date (Figure 8a). In contrast, the Wp311 site (limestone/sandstone) obtained the largest difference from the field data and also, the highest differences between selected aerosol models (see Figure 8b). An explanation for this great difference can be heterogeneity of this site. Because from this comparison we can also see a high deviation of the reference field data and it may be an indication of inhomogeneous surface measurements as well (Figure 8b black spectra). Homogeneity of the reference sites will be discussed later in section 4.4.

Two spectral matching techniques Spectral Angle Mapper (SAM) and Spectral Feature Fitting (SFF) were used to comparing the spectral similarity between image spectra and resampled field spectra of the three reference sites (see Table 8 and Table 9). The resulting highest scores from these two methods were not similar for each site indicating their different approaches to measure the similarity between target and reference spectra. SAM high scores showed its insensitivity to the illumination differences while SFF showed low sensitive results between different aerosol models giving them almost the same scores. Nevertheless, both methods gave the same high score for the spectra from the maritime aerosol model for all three sites. These results show that used methods were not always in good agreement with the visual comparison and suggest a necessity of using alternative methods of spectral similarity measurements.

From visual and spectral similarity comparisons, the maritime aerosol model was selected as an appropriated aerosol model for the study area based on three reference sites results. Though, the urban model showed the minimal difference from the field data in Wp313-314 (FLAASH results) and the rural model gained the highest score from SAM in this site (Figure 8 & Table 9). These results suggest that aerosol model's performance can be variable depending on the surface type. Studies by Nazeer et al. (2014) and Bassani et al. (2012) showed that influences of aerosol models vary with respect to the surface type. In their studies, the urban aerosol model seemed to be more accurate for bright surfaces such as sand which is similar to the site Wp313-314 a sandy beach.

We compared the maritime aerosol model results of ATCOR3 and FLAASH with field resampled data (see Figure 9 & Figure 10). As it was mentioned earlier, regarding spectral shape, the ATCOR3 produced image spectra of the reference sites seemed to be tilted, while the FLAASH corrected image spectra correspond to the shape of the field spectra equally in all bands of WV-3 image. Consequently, the surface reflectance differences between ATCOR3 and the field data deviate gradually in the VNIR and SWIR bands of the image (Figure 10 dark to light blue bars). Lastly, based on visual and direct comparisons of absolute values and spectral matching results, the FLAASH atmospheric correction method was found to produce results closer to the field data than ATCOR3 method for all three sites.

4.2.2. Comparison of May and September WV-3 scenes

The second WV-3 dataset, acquired on 28 May 2017, was processed using ATCOR3 and FLAASH AC methods with maritime aerosol model and compared to the September WV-3 images on the three reference sites (Figure 11). The surfaces of the reference sites are bare ground for Wp333,

limestone/sandstone exposure for Wp311 and sandy beach for Wp313-314 respectively. Hence, we did not expect differences in the reflectance spectra of the sites between two acquisitions. The comparison results showed some variations in all sites. For the ATCOR3 results, overall spectra look similar, but the surface reflectance of the two sites Wp311 and Wp313-314 have been estimated from May image lower than in September scene (Figure 11b-c).

Regarding the FLAASH results comparison, the Wp311 site showed the greatest difference between the two scenes. This large difference at the Wp311 site can be caused by heterogeneity of the area and mismatching between the area measured in the field and the drawn region of interest (ROI) on the image. Because while examining AC results applied on May image, we observed location differences between two scenes and as it was reported in the methodology section, the September image has been shifted by one pixel to the west (see section 2.4.1). Regarding this issue, the heterogeneity of the reference sites and geolocation differences between May and September WV-3 images are included in the next subsections for discussion.

4.2.3.   Comparison between FLAASH, AComp and field data

Since the DigitalGlobe provides an atmospherically corrected reflectance image AComp to end-users, we have added the AComp images to our comparison to see their correspondence with the field spectral measurements. The WV-3 AComp images were provided together with radiance images by DigitalGlobe. The comparisons have been done between the FLAASH corrected images (with maritime aerosol model) and the AComp images for both acquisition dates May and September (see Figure 12).

From both scenes, it is observed that AComp images tend to show continually higher reflectance values at 2329nm than the FLAASH outcomes for all reference sites. Especially in the Wp333 site, a clear difference was observed in this last band for May image (Figure 12a). The FLAASH result showed a small absorption feature in the 2329nm band, whereas the AComp image reflectance value has increased compared to the previous adjacent band's reflectance value for this site. This last band at 2329nm is important for mapping carbonate and Mg-OH bearing minerals as their diagnostic spectral absorption features occur near 2330nm wavelength. Thus, if the AComp tendency of overestimating the last band's value is kept for the entire scene, i.e., for different land covers as well, this might affect the mineral mapping of the area.

On the other hand, the September AComp image spectra (Figure 12d-f) did not exhibit an unknown feature at 824nm and this was consistent with the field data and different to the results of previously compared AC methods including the FLAASH results. The FLAASH method constantly overestimated reflectance at 723nm. Both AComp and FLAASH methods produced higher values at 1730nm than the adjacent 1660nm band of the image, showing a little peak in the spectral shape where the resampled field spectra show a small absorption dip instead. Hence, this problem is most probably related to the WV-3 SWIR4 band itself and not with the used AC methods.

For conclusion and ease of explanation, the results of ATCOR, FLAASH methods and AComp images are plotted together with the field resampled spectra in Appendix 4. All in all, the FLAASH atmospheric correction with the maritime aerosol model was found to produce the closest results to the field. Especially, when we consider the results of the Wp333 site to be the most important results because this site was measured in the field at the same time as the WV-3 September image acquisition. This means environmental and atmospheric conditions of the field data acquisition are the same as the image data and provide us with a more confident comparison opportunity. These results suggest that the ASD measurement method with bare fibreoptic cable is the appropriate method of in-situ spectral measurements for validating atmospheric correction of the remotely sensed images. In this Wp333 site,

the FLAASH estimated surface reflectance spectrum was the best matching spectrum with the field resampled spectrum.

4.3. Geolocation difference between scenes

After inspecting both May and September WV-3 images visually with the assistance of GPS waypoints taken during the field spectral measurement, the May image was found to be closer to the control points (Figure 22). To correct the location differences between the scenes, two methods were tested: image-to-image registration and manual pixel shift in the header file of the image. The former method showed overall 2.1m RMSE accuracy based on 25 ground control points, but after applying this method original reflectance values have been changed due to resampling performed during the process. To overlay the two scenes, we preferred to correct the location difference manually by shifting the September image one pixel (7.5m pixel size) west (in the horizontal direction only) in order to keep the pixel values intact.
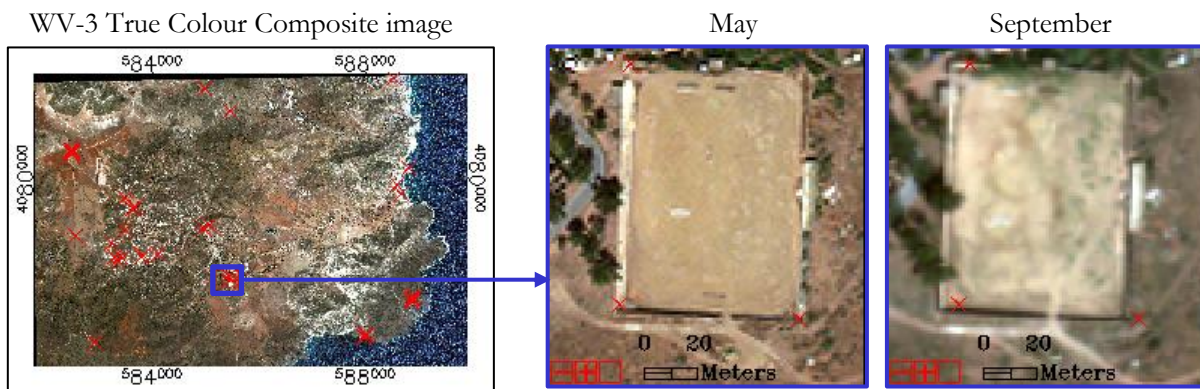
Figure 22. Comparison of May and September VNIR images' geolocation accuracy with field GPS control points (red crosses).

Figure 23 shows a spectral plot of the three sites extracted from FLAASH corrected September image before and after the pixel-shifting of the image. As shown here, the surface reflectance spectrum of the Wp311 site has changed significantly (up to 3%) after applying the pixel shift on September image compared to the other two sites which have differences up to 0.5%. The large difference of the Wp311 site is most likely related to the heterogeneity of the site surface, and this result suggests that geolocation accuracy plays an important role when comparing different scene acquisitions.

WV-3 data is a high spatial resolution data with 0.31m pixel size for the panchromatic image, 1.2m for VNIR image and 7.5m for SWIR image. Horizontal geolocation accuracy <3.5m CE90 (DigitalGlobe, 2019) is poorer compared to the pixel sizes of the image products. According to DigitalGlobe (2010), they offer a 'Custom Orthorectified Image' product in which they use a customer-provided support data of DEM or Ground Control Points. The suggested horizontal accuracy of the required support data is 70cm RMSE and 125cm RMSE of vertical accuracy. Since WV-3 is a commercial satellite data, it is recommended to purchase WV-3 image with supporting files in order to benefit from its high spatial resolution images with accurate geocorrection.
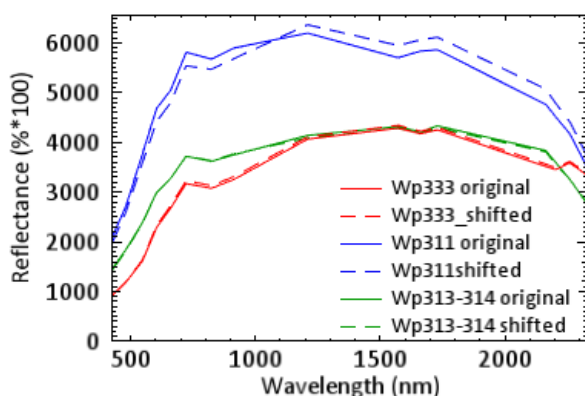
Figure 23. Spectral profile of the reference sites before and after correcting geolocation difference.

4.4. Homogeneity of the reference site surfaces

To investigate homogeneity of surface cover of the reference sites, first, September WV-3 image with 16 bands was subset to the extent of the reference sites Wp333 and Wp311 excluding Wp313-314 site. The Wp313-314 site was drawn as a line ROI and was found to have relatively consistent results thus, it has not been examined for homogeneity. Then, the multispectral edge filter using Euclidean Distance (ED) measure in HypPy3 software was applied on the subset images (Bakker & Schmidt, 2002). This filter with ED measure is a combination of edge filters using Spectral Angle (SA) and Intensity Difference (ID) measures and identifies all features detected by SA and ID edge filters (Bakker & Schmidt, 2002).
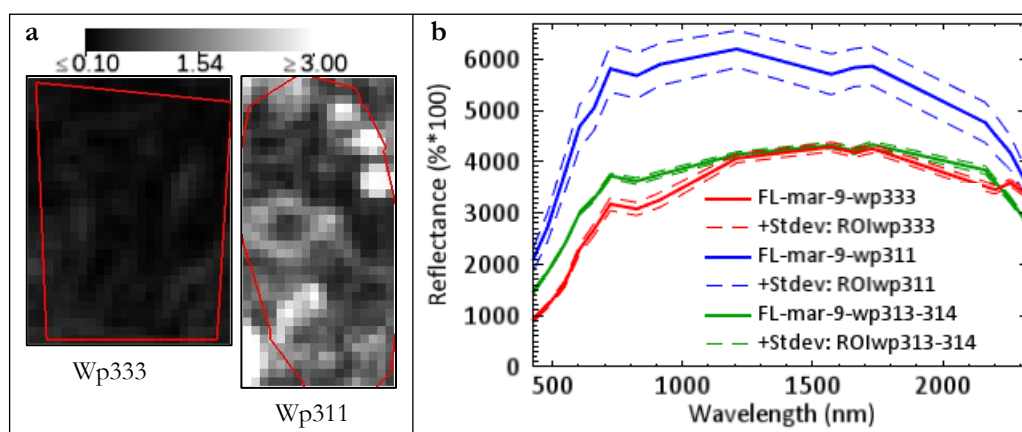
Figure 24. a) Edge filtering results applied on Wp333 and Wp311 sites subset images. Red lines represent boundary of the ROIs of the sites. b) Reference site spectra and their standard deviations retrieved from FLAASH corrected September image.

As a result, shown in Figure 24, clear, sharp edge differences are detected in the Wp311 site while the Wp333 site result has subtle edge differences with almost homogeneous dark image. The mean value of the Wp333 site is 0.27 and 1.11 for the Wp311 site. Figure 24b shows the mean spectra of the three reference sites and their standard deviations retrieved from FLAASH corrected image. The edge filtering mean values and the standard deviations of the mean spectra of the sites suggest that Wp311 reference site has the most heterogeneous surface.

The results of homogeneity of the reference sites and geocorrection accuracy of the scenes suggest that they can play an essential role in the large differences observed between image and field data as well.

4.5. Mineral mapping results

The final objective of this research was to evaluate differences in mineral maps due to applying different atmospheric correction methods. For this purpose, the AComp image and FLAASH corrected image from two acquisitions were analysed by using band ratio techniques and the SAM method to map alteration minerals in Rodalquilar.

4.5.1. Band ratio results

Two different sets of band ratios were used to map well-exposed alteration minerals such as kaolinite, alunite, illite and calcite in the study area: 1) three mineral indices by Sun et al. (2016) for WV-3 bands and 2) three band ratios by Rowan (Aleks & Oliver, 2004) for ASTER bands (see Table 7). Before processing the images, the vegetation effect was suppressed by masking pixels with NDVI values less than 0 and greater than 0.4 based on the vegetation analysis by Usman (2018). The comparisons of the band ratio products were done visually and as scatterplots (Figure 14 &Figure 13).

The Sun's three mineral indices (kaolinite, Al-OH, and calcite) showed very high correlations of 0.99 between the May-AComp and the May-FLAASH results (see Figure 14- the top two rows & Figure 13-a,c,e). Nevertheless, their value ranges varied significantly between AComp and FLAASH outcomes. This difference in value range is most likely caused by the last band at 2329nm in AComp image. The previous spectral comparison results showed AComp's tendency to have relatively higher reflectance in the 2329nm band of WV-3. On the other hand, the mineral index maps from the September scene showed lower correlations with wider data clusters except for the calcite index maps (see Figure 14- the bottom two rows & Figure 13-b,d,f). The kaolinite and Al-OH index maps were influenced by the striping effect of the September AComp data, while the calcite distribution is not falling in the area of image striping (Figure 14-the bottom two rows). This can be the reason for the lower correlation of the kaolinite and Al-OH maps and high correlation of the calcite maps from September scene. Sun et al. mineral indices results appeared to be affected severely by the band combinations in their formulas. As all the formulas involve the last band at 2329nm (see section 3.3.1 - S8 in the formula), when it is in the denominator of the formula (Al-OH and calcite indices), it tends to predict lower mineral abundances (Figure 14: e & i).

Therefore, to avoid this one band dependence we tried another well-established set of band ratios for ASTER defined by Rowan (Aleks & Oliver, 2004) and adapted them to the WV-3 bands. Most of the WV-3 SWIR bands are similar to ASTER SWIR bands (Table 7). The used three band ratios (relative band depth) are: 1) alunite/kaolinite/pyrophyllite [(S3+S6)/S5 or (1661nm+2202nm)/2163nm]; 2) sericite/illite/smectite [(S5+S7)/S6 or (2163nm+2259nm)/2202nm]; and 3) dolomite [(S6+S8)/S7 or (2202nm+2329nm)/2259nm] (Figure 16 & Figure 15). They have been selected based on their similarity of discriminating mineral types with Sun's mineral indices.

Generally, the illite/smectite ratio images showed the highest correlations in both scenes and had the least differences between AComp and FLAASH outcomes (Figure 16- the second column & Figure 15c-d). However, there was a confusion between illite ratio results and agricultural fields/bare soils pixel values in the west-north of the image. This was due to a spectral similarity with montmorillonite in the soil that has a weak absorption feature at 2202nm (Clark, 1999) and shoulders at 2163nm and 2259nm – the bands in the ratio formula. In contrast, the dolomite ratio image from May acquisition had the largest difference between AComp and FLAASH corrected images (Figure 16i & j). This result confirmed the AComp's issue on the last 2329nm band and high reflectance values in this last band (S8 in the ratio formula) showed relatively intense dolomite image. Regarding the kaolinite/alunite/pyrophyllite ratio images, visible differences occurred between the two scenes and mineral prediction is likely to be more abundant in September images (Figure 16c & d). The September AComp result was affected by striping same as Sun's

kaolinite and Al-OH index maps. It is likely that one of the three bands involved in band combinations is also suffering from the striping effect.

4.5.2.   SAM mineral mapping results

The SAM mapping method was applied on the AComp image, and FLAASH corrected images from May and September dates. For each image, a separate endmember collection was used for the classification, but the endmember spectra were extracted from the same locations of the mineralisation (Figure 17). To obtain more accurate classification results, the WV-3 input images were spectrally subset to SWIR bands (SWIR1–SWIR8 bands in the 1209nm-2329nm region), in order to only focus on diagnostic absorption features of the selected endmember minerals.

The SAM classification was applied with two different thresholds for all endmembers uniformly: 0.1radians (the maximum acceptable angle difference between image and reference spectra) and 10% of the rule-image histogram. The SAM results of default threshold 0.1radians (Figure 18) showed similar overall results between AComp and FLAASH outcomes, but significant difference in mineral abundances between May and September scenes. The calcite was overpredicted covering the almost entire scene in each AComp and the FLAASH images of two dates. This is caused probably, because of the uniformly selected threshold value for all endmembers. Besides, the illite abundance varied significantly between AComp and FLAASH images. Particularly, for September illite results, they have been affected by the striping effect of the AComp image.

The results of post-classification using rule images of the endmembers with a 10% of the rule-image histogram threshold were unexpected (Figure 20 & Figure 21). The spatial distribution and percentage abundance of the minerals have become more similar and closer between all four images compared to the previous results. Especially, illite abundances were around 12% in May images and 16%-21% in September images (Figure 19). However, after applying the 10% threshold, these values dropped to 6% similarly for all four images (Figure 21). For alunite in May-AComp image, it was detected in the southern part of the area having 6.8% higher than three other images, while after changing the threshold it became 2.6% more closer to the other results. Most likely alunite in the southern part was misclassification (false anomalies).

For the final discussion about mineral mapping results, colour composite images (CCI) of the band ratio results and mineral map by SAM produced from the September FLAASH image were compared with the published geological map of Rodalquilar by Arribas (1993). The SAM result with a 10% threshold value is presented for the comparison (Figure 25a). In Figure 25b, a ratio colour composite image of Sun's mineral indices is shown in RGB: R=kaolinite, G=Al-OH, B=calcite. Similarly, in Figure 25d the Rowan's three ratios are shown in RGB as well: R=kao/alun, G=illite/smec, B=dolomite.

Overall, Sun's calcite index worked well in colour composite highlighting limestones at the eastern part of the study area (Figure 25: b-blue tone & c-unit 19) whereas the Rowan's dolomite ratio image appeared to show larger areas than it is expected in the territory (Figure 25: d-purple tone). This could be due to its spectral similarity (in the selected three bands of the ratio) with dry vegetation that is abundant in the study area (Bedini et al., 2009; Usman, 2018). Rowan's two other ratio images showed kaolinite/alunite as red-yellow colour and illite exposure as green but there is confusion with agricultural areas in the west-north (Figure 25d). Sun's kaolinite and Al-OH predictions were overlapped in the same place and reflected as yellow colour on the map. The SAM classified mineral map (Figure 25a) showed a relatively similar pattern of kaolinite and illite with the greenish colour of the CCI made of Rowan's ratios (Figure 25d) in the eastern part of the image. Whereas the calcite class (cyan coloured class in Figure 25a) has a similar

spatial pattern with the blue colour of the CCI made of Sun's indices (Figure 25b) and the orange unit-19 of the Arribas' geologic map in the eastern part as well (Figure 25c).
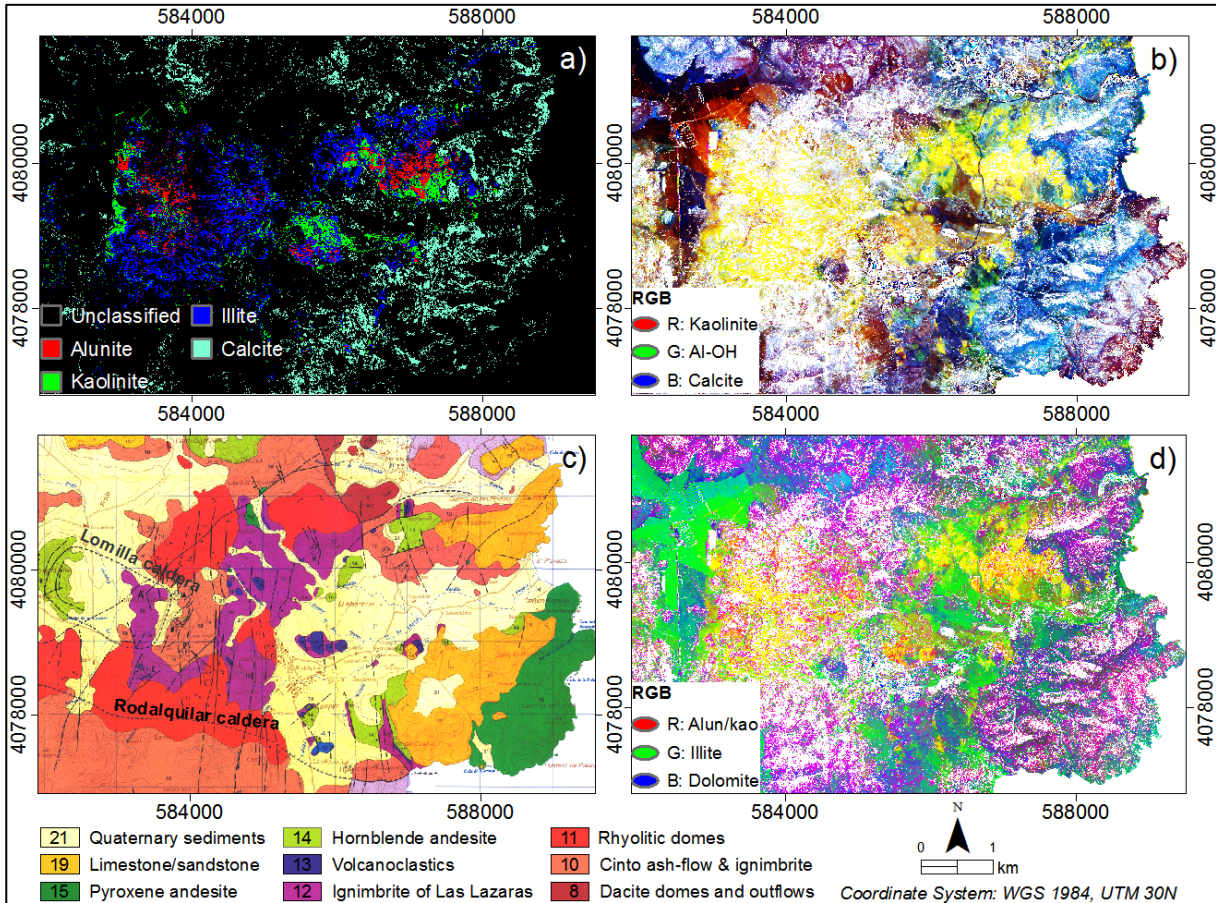

Figure 25. Comparison of geological map with the mineral maps produced from the band ratios and the classification using SAM. a) SAM classified image with 10% threshold, b) A colour composite image made of Sun's mineral indices, c) Arribas' geological map, and d) A colour composite image made of Rowan's band ratios.

To summarise, atmospheric corrections resulting in an effect on specific bands, for instance, tendency of ATCOR and AComp to overestimate reflectance in the first and last bands of WV-3 respectively, can influence ratio images and may lead to an over or underprediction of minerals. The used three mineral indices by Sun et al. (2016) appeared to be affected severely by the last S8 band involved in all the formulas. SAM method produced inconsistent results depending on the used threshold values, and the use of different input reflectance images appeared to have less influence on the produced mineral maps. Therefore, it is more important for mineral mapping to select a reliable classification method rather than to select an appropriate atmospheric correction method.

For the conclusion of this chapter, we made a table listing the problems and consequences discussed in this chapter that made complicated to compare and obtain consistent results of the atmospheric corrections and mineral mapping (see Table11). Considering all these consequences, it appears to be difficult to compare and determine the best performing atmospheric correction method.

Table 11. List of issues related to the dataset and methods used in this study.

	Problems	Descriptions
1	Different versions of the satellite datasets	The September images have two different radiance images the original and recalibrated
2	Different methods of the field spectral measurements	Wp333 was measured by using bare fiberoptic cable while the other sites were measured with a contact probe
3	Geolocation differences between two scenes	The September images were shifted by one pixel which is 7.5m
4	Heterogeneity of the reference sites	The Wp311 appeared to be more heterogeneous than the other two sites having large deviations in the field and image spectra
5	Satellite dataset quality	The September images were affected by striping
6	Issues of band ratio techniques	The used Sun's three mineral indices were affected by the last S8 band fixed in all the formulas.
7	Issues of mineral mapping by SAM	SAM produces inconsistent classification results depending on the used threshold values

5.   CONCLUSIONS AND RECOMMENDATIONS

This research aimed to determine the most suitable atmospheric correction method for WorldView-3 satellite image. This study involved two modules of ATCOR (ATCOR2 and ATCOR3) and FLAASH atmospheric corrections on WV-3 images and evaluated their accuracy using ground truth measurements. The WV-3 satellite images were acquired in May and September 2017 over Rodalquilar, southeast Spain. As Rodalquilar hosts different hydrothermal alteration zones that consist of VNIR and SWIR active minerals, this study also sought to know whether different atmospheric corrections can influence mineral mapping results. Our results of AC comparisons and mineral mapping lead to the following conclusions:

- One of the most important atmospheric conditions parameters is the aerosol type of the area. Results of the tested three aerosol models showed that the urban aerosol model causes overestimation of reflectance due to its composition of more absorbing water-soluble components. Especially, this was seen in the ATCOR2 result that has differences up to 25% from the field spectra, and the spectral shape is quite different in the VNIR region. Regarding the software settings, in ATCOR algorithm, the use of separate processing steps of the VNIR and SWIR images of WV-3 may cause the observed tilt of the spectra in these regions. This tilting should be investigated further as it appeared in all reference sites and caused a significant difference from the field data.

- Our results showed that the reflectance image spectra of the reference sites did exhibit unknown features that are not present in the field spectra. The wavelengths of the bands that have these features in the image spectra are at 427nm, 824nm, 1661nm-1730nm, and 2329nm. The unknown features that occurred in the two adjacent bands at 1661nm and 1730nm were present in all image spectra which were derived from ATCOR, FLAASH and AComp. This result suggests that it is probably related to the WV-3 satellite dataset itself and should be inspected further.

- For the band ratio techniques, differences were observed in value ranges and mineral abundances. The former is caused mostly by AComp's tendency of overestimating reflectance in the last 2329nm band, and the latter is mainly due to the striping effect in the September AComp image. SAM classification results using two different thresholds showed quite different results. The differences were caused by the applied threshold values but are not due to different input reflectance images.

- The image reflectance data of the Wp333 site showed results closest to the field spectral measurements for all tested AC methods. The use of ASD bare fibreoptic cable measurements that were used in this site had several advantages over using contact probe measurements in the other areas: a) measurements were done simultaneously with the image data acquisition, b) the light source was the same as the image data – the sunlight, b) a larger areal coverage on the ground, and c) the use of multiple and systematic gridded measurements. With these advantages, we conclude that this method was the most appropriate method of validating atmospheric correction results of remotely sensed images.

To summarise, this study was the first to our knowledge to evaluate different atmospheric correction methods using WV-3 satellite image. However, it should be noted that during this study as discussed earlier, we encountered a number of problems and consequences that made AC comparisons complicated. Some of these problems are different versions of the same dataset, geolocation difference, striping effect, and different methods of field spectral measurements. On the other hand, these results and consequences

contribute to understand potential issues and sources of errors in reflectance image and mineral maps and to select the optimal method of AC and mineral mapping using WV-3 image. Overall, the FLAASH method was the most accurate for all the selected reference sites outperforming other methods and was highly accurate over the site Wp333 that was measured at the same time of WV-3 image acquisition.

Based on the conclusions drawn above, the following recommendations are made:

- For further application of atmospheric correction methods, the ATCOR's empirical approach of computing reflectance in the deep blue channel should be re-evaluated as there were obvious differences in all selected sites compared to other AC methods and field data.

- We recommend trying to apply the ATCOR algorithm on a VNIR, and SWIR combined WV-3 image with aerosol retrieval using all bands in these regions together. This may help to solve obtaining a tilted reflectance spectrum.

LIST OF REFERENCES

Abreu, L. W., Anderson, G. P., Chetwynd, J. H., & Berk, A. (1996). *The MODTRAN 2/3 Report and LOWTRAN 7 MODEL. Ontar Corporation for PL/GPOS*.

Aleks, K., & Oliver, S. (2004). ASTER Mineral Index Processing Manual. *Remote Sensing Applications Geoscience Australia*, (October 2004).

Anderson, G. P., Pukall, B., Allred, C. L., Jeong, L. S., Hoke, M., Chetwynd, J. H., … Matthew, M. W. (1999). FLAASH and MODTRAN4: state-of-the-art atmospheric correction for hyperspectral data. In *1999 IEEE Aerospace Conference. Proceedings (Cat. No.99TH8403)* (pp. 177–181 vol.4). IEEE. https://doi.org/10.1109/AERO.1999.792088

Arribas, A. (1993). *Mapa geológico del distrito minero de Rodalquilar, Almería*. Madrid, Spain: Instituto Tecnologico GeoMinero de Espana.

Arribas, A., Cunningham, C. G., Rytuba, J. J., Rye, R. O., Kelly, W. C., Podwysocki, M. H., … Tosdal, R. M. (1995). Geology, geochronology, fluid inclusions, and isotope geochemistry of the Rodalquilar gold alunite deposit, Spain. *Economic Geology*, *90*(4), 795–822. https://doi.org/10.2113/gsecongeo.90.4.795

Asadzadeh, S., & de Souza Filho, C. R. (2016). A review on spectral processing methods for geological remote sensing. *International Journal of Applied Earth Observation and Geoinformation*, *47*, 69–90. https://doi.org/10.1016/J.JAG.2015.12.004

Ayoobi, I., & Tangestani, M. H. (2017). Evaluation of relative atmospheric correction methods on ASTER VNIR–SWIR data in playa environment. *Carbonates and Evaporites*, *32*(4), 539–546. https://doi.org/10.1007/s13146-016-0316-3

Bakker, W. H., & Schmidt, K. S. (2002). Hyperspectral edge filtering for measuring homogeneity of surface cover types. *ISPRS Journal of Photogrammetry and Remote Sensing*, *56*(4), 246–256. https://doi.org/10.1016/S0924-2716(02)00060-6

Barazzetti, L., Roncoroni, F., Brumana, R., & Previtali, M. (2016). Georeferencing accuracy analysis of a single WorldView-3 image collected over Milan. *International Archives of the Photogrammetry, Remote Sensing and Spatial Information Sciences - ISPRS Archives*, *XLI-B1*(July), 429–434. https://doi.org/10.5194/isprsarchives-XLI-B1-429-2016

Bassani, C., Cavalli, R. M., & Antonelli, P. (2012). Influence of aerosol and surface reflectance variability on hyperspectral observed radiance. *Atmospheric Measurement Techniques*, *5*(6), 1193–1203. https://doi.org/10.5194/amt-5-1193-2012

Bedini, E., Van der Meer, F., & Van Ruitenbeek, F. (2009). Use of HyMap imaging spectrometer data to map mineralogy in the Rodalquilar caldera, southeast Spain. *International Journal of Remote Sensing*, *30*(2), 327–348. https://doi.org/10.1080/01431160802282854

Ben-Dor, E., Kindel, B., & Goetz, A. F. H. (2004). Quality assessment of several methods to recover surface reflectance using synthetic imaging spectroscopy data. *Remote Sensing of Environment*, *90*(3), 389–404. https://doi.org/10.1016/j.rse.2004.01.014

Clark, R. N. (1999). Spectroscopy of rocks and minerals, and principles of spectroscopy. In *Manual of Remote Sensing, Volume 3, Remote Sensing for the Earth Sciences* (pp. 3–58). New York: John Wiley and Sons.

Clark, R. N., Swayze, G. A., Livo, K. E., Kokaly, R. F., King, T. V. V., Dalton, J. B., … McDougal, R. R. (2002). Surface reflectance calibration of terrestrial imaging spectroscopy data: a Tutorial using AVIRIS. In *Proceedings of the 10th Airborne Earth Science Workshop*. JPL Publication 02-1. Retrieved from ftp://popo.jpl.nasa.gov/pub/docs/workshops/02_docs/2002_Clark_web.pdf

Crowley, J. K., Brickey, D. W., & Rowan, L. C. (1989). Airborne imaging spectrometer data of the Ruby Mountains, Montana: Mineral discrimination using relative absorption band-depth images. *Remote Sensing of Environment*, *29*(2), 121–134. https://doi.org/10.1016/0034-4257(89)90021-7

CustomWeather. (2019). Climate & Weather Averages in Almería, Spain. Retrieved February 14, 2019, from https://www.timeanddate.com/weather/spain/almeria/climate

DigitalGlobe. (2010). *Specifications for Customer-Provided Support Data*. Retrieved from https://dg-cms-uploads-production.s3.amazonaws.com/uploads/document/file/103/Specifications-Customer_Provided_Support_Data.pdf

DigitalGlobe. (2016). *DigitalGlobe Atmospheric Compensation*. Retrieved from http://digitalglobe-marketing.s3.amazonaws.com/files/documents/AComp_WP_ACOMP.pdf

DigitalGlobe. (2019). Satellite Information - DigitalGlobe. Retrieved February 24, 2019, from https://www.digitalglobe.com/resources/satellite-information

Erlick, C., & Frederick, J. E. (1998). Effect of aerosols on the wavelength dependence of atmospheric transmission in the ultrviolet and visible 2. Continental and urban aerosols in clear skies. *Journal of Geophysical Research*, *103*(D18), 23275–23285.

Gao, B.-C., & Davis, C. O. (1997). Development of a line-by-line-based atmosphere removal algorithm for airborne and spaceborne imaging spectrometers. *Proceedings of the Society of Photo-Optical Instrumentation Engineers (SPIE)*, *3118*(October 1997), 132–141. https://doi.org/10.1117/12.283822

Gao, B. C., Montes, M. J., Davis, C. O., & Goetz, A. F. H. (2009). Atmospheric correction algorithms for hyperspectral remote sensing data of land and ocean. *Remote Sensing of Environment*, *113*(SUPPL. 1), S17–S24. https://doi.org/10.1016/j.rse.2007.12.015

Goetz, A. F. H., Kindel, B. C., Ferri, M., & Gutmann, E. (2003). Relative performance of HATCH and three other techniques for atmospheric correction of Hyperion and AVIRIS data. In *12th JPL Airborne Earth Science Workshop*. Pasadena, CA, United States: Jet Propulsion Lab., California Inst. of Tech. Retrieved from ftp://popo.jpl.nasa.gov/pub/docs/workshops/03_docs/Goetz_AVIRIS_2003_web.pdf

Gupta, R. P. (2018). *Remote Sensing Geology* (3rd ed.). Berlin, Germany: Springer Berlin Heidelberg. https://doi.org/10.1007/978-3-662-55876-8

Harris Geospatial Solutions. (2018a). Fast Line-of-sight Atmospheric Analysis of Hypercubes (FLAASH). Retrieved August 22, 2018, from https://www.harrisgeospatial.com/docs/FLAASH.html

Harris Geospatial Solutions. (2018b). *Hyperspectral Analysis: SAM and SFF Tutorial*. Retrieved from http://www.harrisgeospatial.com/portals/0/pdfs/WholePixelHyperspectralAnalysisTutorial.pdf

Hecker, C., Van Der Meijde, M., Van Der Werff, H., & Van Der Meer, F. D. (2008). Assessing the influence of reference spectra on synthetic SAM classification results. *IEEE Transactions on Geoscience and Remote Sensing*, *46*(12), 4162–4172. https://doi.org/10.1109/TGRS.2008.2001035

Janzen, D. T., Fredeen, A. L., & Wheate, R. D. (2006). Radiometric correction techniques and accuracy assessment for Landsat TM data in remote forested regions. *Canadian Journal of Remote Sensing*, *32*(5), 330–340. https://doi.org/10.5589/m06-028

Kale, K. V., Solankar, M. M., Nalawade, D. B., Dhumal, R. K., & Gite, H. R. (2017). A Research review on hyperspectral data processing and analysis algorithms. *Proceedings of the National Academy of Sciences, India Section A: Physical Sciences*, *87*(4), 541–555. https://doi.org/10.1007/s40010-017-0433-y

Kawishwar, P. (2007). *Atmospheric Correction Models for Retrievals of Calibrated Spectral Profiles from Hyperion EO-1 Data*. The International Institute of Geo-Information Science and Earth Observation, Enschede, The Netherlands. Retrieved from http://www.itc.nl/library/papers_2007/msc/iirs/kawishwar.pdf

Kruse, F. A. (2004). Comparison of ATREM, ACORN and FLAASH atmospheric corrections using low-altitude AVIRIS data of Boulder, Colorado. In *Proceedings of 13th JPL Airborne Geoscience Workshop* (pp. 1–10). Pasadena, CA, USA. Retrieved from https://www.researchgate.net/profile/F_Kruse/publication/228699945_Comparison_of_ATREM _ACORN_and_FLAASH_atmospheric_corrections_using_low-altitude_AVIRIS_data_of_Boulder_CO/links/00b4953835db0a0393000000/Comparison-of-ATREM-ACORN-and-FLAASH-atmospheric-co

Kruse, F. A., Baugh, W. M., & Perry, S. L. (2015). Validation of DigitalGlobe WorldView-3 Earth imaging satellite shortwave infrared bands for mineral mapping. *Journal of Applied Remote Sensing*, *9*(May 2015), 096044. https://doi.org/10.1117/1.JRS.9.096044

Kruse, F. A., Lefkoff, A. B., Boardman, J. W., Heidebrecht, K. B., Shapiro, A. T., Barloon, P. J., & Goetz, A. F. H. (1993). The spectral image processing system (SIPS)—interactive visualization and analysis of imaging spectrometer data. *Remote Sensing of Environment*, *44*(2–3), 145–163. https://doi.org/10.1016/0034-4257(93)90013-N

Kruse, F. A., & Perry, S. L. (2013). Mineral mapping using simulated worldview-3 short-wave-infrared imagery. *Remote Sensing*, *5*(6), 2688–2703. https://doi.org/10.3390/rs5062688

Kuester, M. (2016). *Radiometric use of WorldView-3 imagery*. Retrieved from https://dg-cms-uploads-production.s3.amazonaws.com/uploads/document/file/207/Radiometric_Use_of_WorldView-3_v2.pdf

Manakos, I., Manevski, K., Kalaitzidis, C., & Edler, D. (2011). Comparison between FLAASH and ATCOR atmospheric correction modules on the basis of Worldview-2 Imagery and in situ spectroradiometric measurements. *EARSeL 7th SIG-Imaging Spectroscopy Workshop*, (11–13 April), 11. Retrieved from

http://www.earsel2011.com/content/download/Proceedings/S12_4_Manakos_paper.pdf

Miller, C. J. (2002). Performance assessment of ACORN atmospheric correction algorithm. *Algorithms and Technologies for Multispectral, Hyperspectral, and Ultraspectral Imagery Viii*, *4725*(August 2002), 438–449. https://doi.org/10.1117/12.478777

NASA. (2019). MODIS Atmosphere. Retrieved February 17, 2019, from https://modis-images.gsfc.nasa.gov/index.html

National Geographic Center (CNIG). (2018). CNIG Download Center (IGN). Retrieved August 17, 2018, from http://centrodedescargas.cnig.es/CentroDescargas/index.jsp#

Nazeer, M., Nichol, J. E., & Yung, Y.-K. (2014). Evaluation of atmospheric correction models and Landsat surface reflectance product in an urban coastal environment. *International Journal of Remote Sensing*, *35*(16), 6271–6291. https://doi.org/10.1080/01431161.2014.951742

Oepen, P. S., Friedrich, G., & Vogt, J. H. (1989). Fluid evolution, wallrock alteration, and ore mineralization associated with the Rodalquilar epithermal gold-deposit in southeast Spain. *Mineralium Deposita*, *24*(4), 235–243. https://doi.org/10.1007/BF00206385

Oyarzun, R., Cubas, P., Higueras, P., Lillo, J., & Llanos, W. (2009). Environmental assessment of the arsenic-rich, Rodalquilar gold–(copper–lead–zinc) mining district, SE Spain: data from soils and vegetation. *Environmental Geology*, *58*(4), 761. https://doi.org/10.1007/s00254-008-1550-3

Perkins, T., Adler-Golden, S. M., Matthew, M. W., Berk, A., Bernstein, L. S., Lee, J., & Fox, M. (2012). Speed and accuracy improvements in FLAASH atmospheric correction of hyperspectral imagery. *Optical Engineering*, *51*(11), 111707. https://doi.org/10.1117/1.OE.51.11.111707

Perkins, T., Adler-Golden, S., Matthew, M., Berk, A., Anderson, G., Gardner, J., & Felde, G. (2005). Retrieval of atmospheric properties from hyper and multispectral imagery with the FLAASH atmospheric correction algorithm. In K. Schäfer, A. Comerón, J. R. Slusser, R. H. Picard, M. R. Carleer, & N. I. Sifakis (Eds.) (p. 59790E). https://doi.org/10.1117/12.626526

Qu, Z., Kindel, B. C., & Goetz, A. F. H. (2003). The high accuracy atmospheric correction for hyperspectral data (HATCH) model. *IEEE Transactions on Geoscience and Remote Sensing*, *41*(6 PART I), 1223–1231. https://doi.org/10.1109/TGRS.2003.813125

Richter, R. (1997). Correction of atmospheric and topographic effects for high spatial resolution satellite imagery. *International Journal of Remote Sensing*, *18*(5), 1099–1111. https://doi.org/10.1080/014311697218593

Richter, R. (2018). *ATCOR Workflow for IMAGINE 2018 User Manual* (Version 1.). Germering, Germany: Geosystems GmbH. Retrieved from https://www.geosystems.de/fileadmin/redaktion/Software/ATCOR_Workflow/ATCOR-Workflow-for-IMAGINE_Help.pdf

Richter, R., & Schläpfer, D. (2002). Geo-atmospheric processing of airborne imaging spectrometry data. Part 2: Atmospheric/topographic correction. *International Journal of Remote Sensing*, *23*(13), 2631–2649. https://doi.org/10.1080/01431160110115834

Richter, R., & Schläpfer, D. (2018). *Atmospheric / Topographic Correction for Satellite Imagery (ATCOR - 2/3 User Guide)* (9.2.0). ReSe Applications LLC. https://doi.org/10.1017/CBO9781107415324.004

Rytuba, J. J., Arribas, A., Cunningham, C. G., McKee, E. H., Podwysocki, M. H., Smith, J. G., … Arribas, A. (1990). Mineralized and unmineralized calderas in Spain; Part II, evolution of the Rodalquilar caldera complex and associated gold-alunite deposits. *Mineralium Deposita*, *25*(S1), S29–S35. https://doi.org/10.1007/BF00205247

San, B. T., & Suzen, M. L. (2010). Evaluation of different atmospheric correction algorithms for EO-1 Hyperion imagery. *International Archives of the Photogrammetry, Remote Sensing and Spatial Information Science*, *XXXVIII*, 392–397.

Sun, Y., Tian, S., & Di, B. (2016). Extracting mineral alteration information using WorldView-3 data. *Geoscience Frontiers*, *8*(5), 1051–1062. https://doi.org/10.1016/j.gsf.2016.10.008

Tempfli, K., Kerle, N., Huurneman, G. C., & Jansen, L. L. F. (2009). *Principles of Remote Remote Sensing - An introductory text book* (4th ed.). Enschede, The Netherlands: The International Institute for Geo-Information Science and Earth Observation (ITC).

Tirelli, C., Curci, G., Manzo, C., Tuccella, P., & Bassani, C. (2015). Effect of the aerosol model assumption on the atmospheric correction over land: Case studies with CHRIS/PROBA hyperspectral images over Benelux. *Remote Sensing*, *7*(7), 8391–8415. https://doi.org/10.3390/rs70708391

Usman, M. S. (2018). *Evaluating ASTER and WorldView-3 mineral mapping capabilities in an epithermal alteration system*. University of Twente, Enschede, The Netherlands. Retrieved from https://library.itc.utwente.nl/login/2018/msc/aes/usman.pdf

Van der Meer, F., Kopačková, V., Koucká, L., Van der Werff, H. M. A., Van Ruitenbeek, F. J. A., & Bakker, W. H. (2018). Wavelength feature mapping as a proxy to mineral chemistry for investigating geologic systems: An example from the Rodalquilar epithermal system. *International Journal of Applied Earth Observation and Geoinformation*, *64*(July 2017), 237–248. https://doi.org/10.1016/j.jag.2017.09.008

Van der Werff, H., & Van der Meer, F. (2016). Sentinel-2A MSI and Landsat 8 OLI provide data continuity for geological remote sensing. *Remote Sensing*, *8*(11), 883. https://doi.org/10.3390/rs8110883

Ye, B., Tian, S., Ge, J., & Sun, Y. (2017). Assessment of WorldView-3 data for lithological mapping. *Remote Sensing*, *9*(11), 1–19. https://doi.org/10.3390/rs9111132

APPENDICES

Appendix 1. Flowchart of the research methodology.
Main steps carried out in the research are illustrated by dashed lines. The datasets used in the study are highlighted by grey colour.
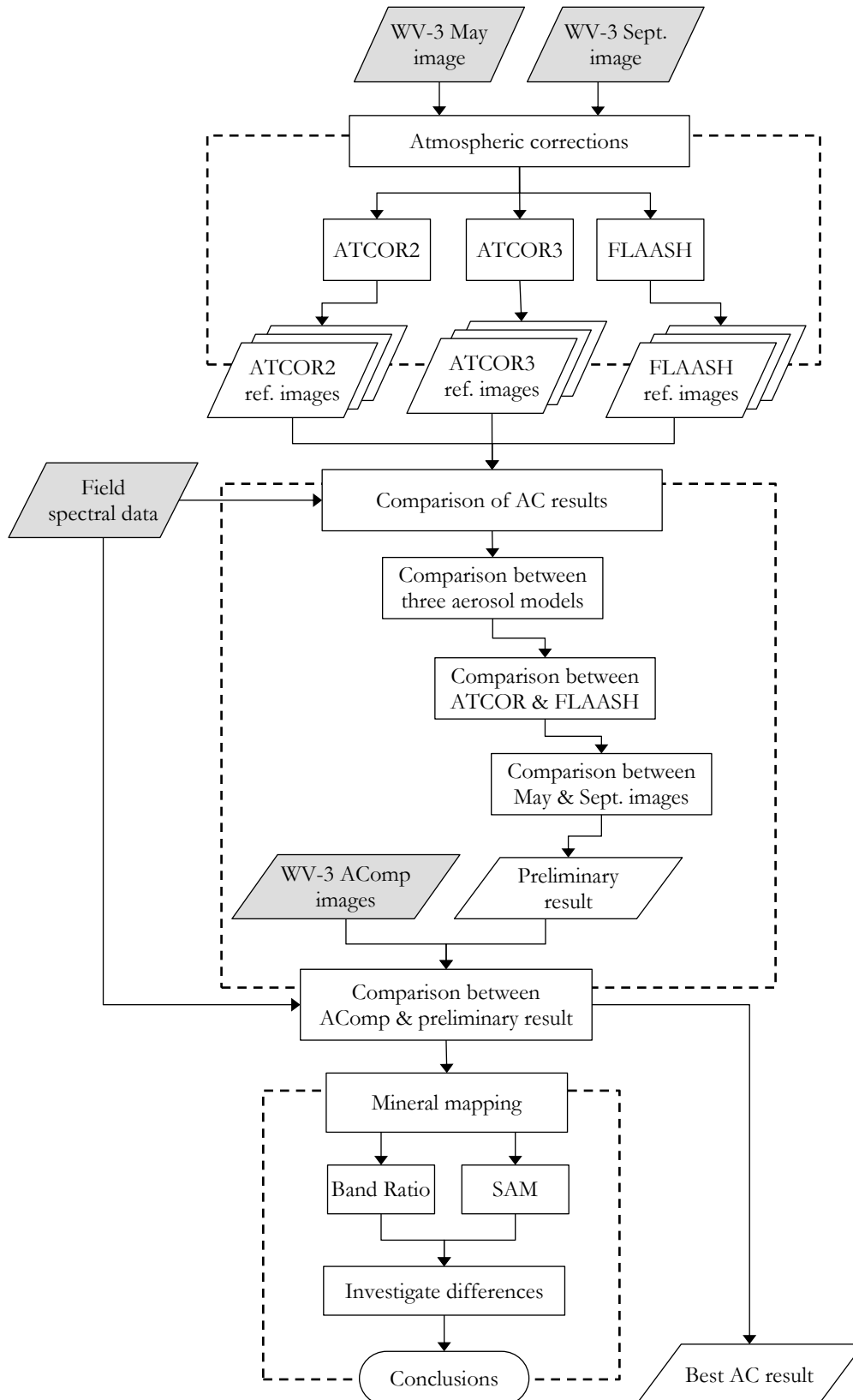
Appendix 2. ATCOR and FLAASH results for the additional target areas.

The surface reflectance spectra of the additional target areas collected from the images corrected by using ATCOR2, ATCOR3, and FLAASH atmospheric correction methods.
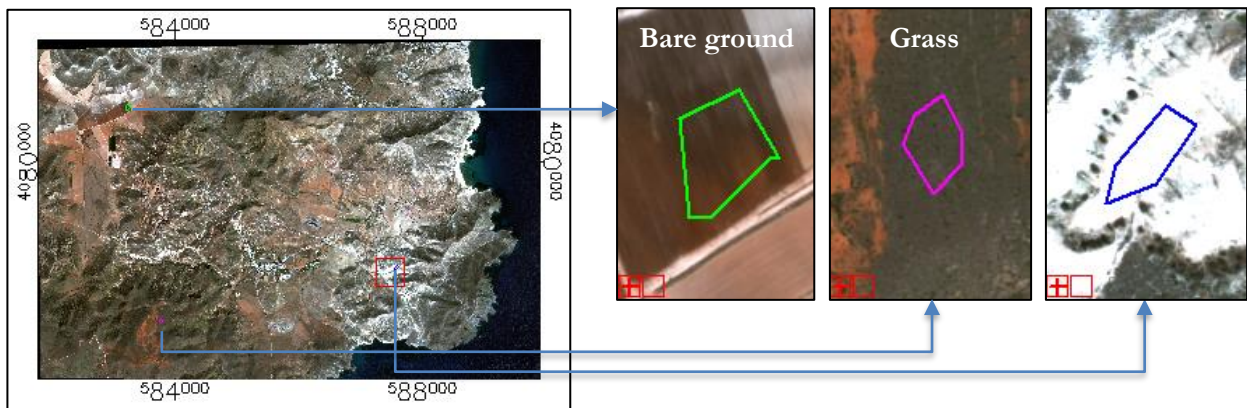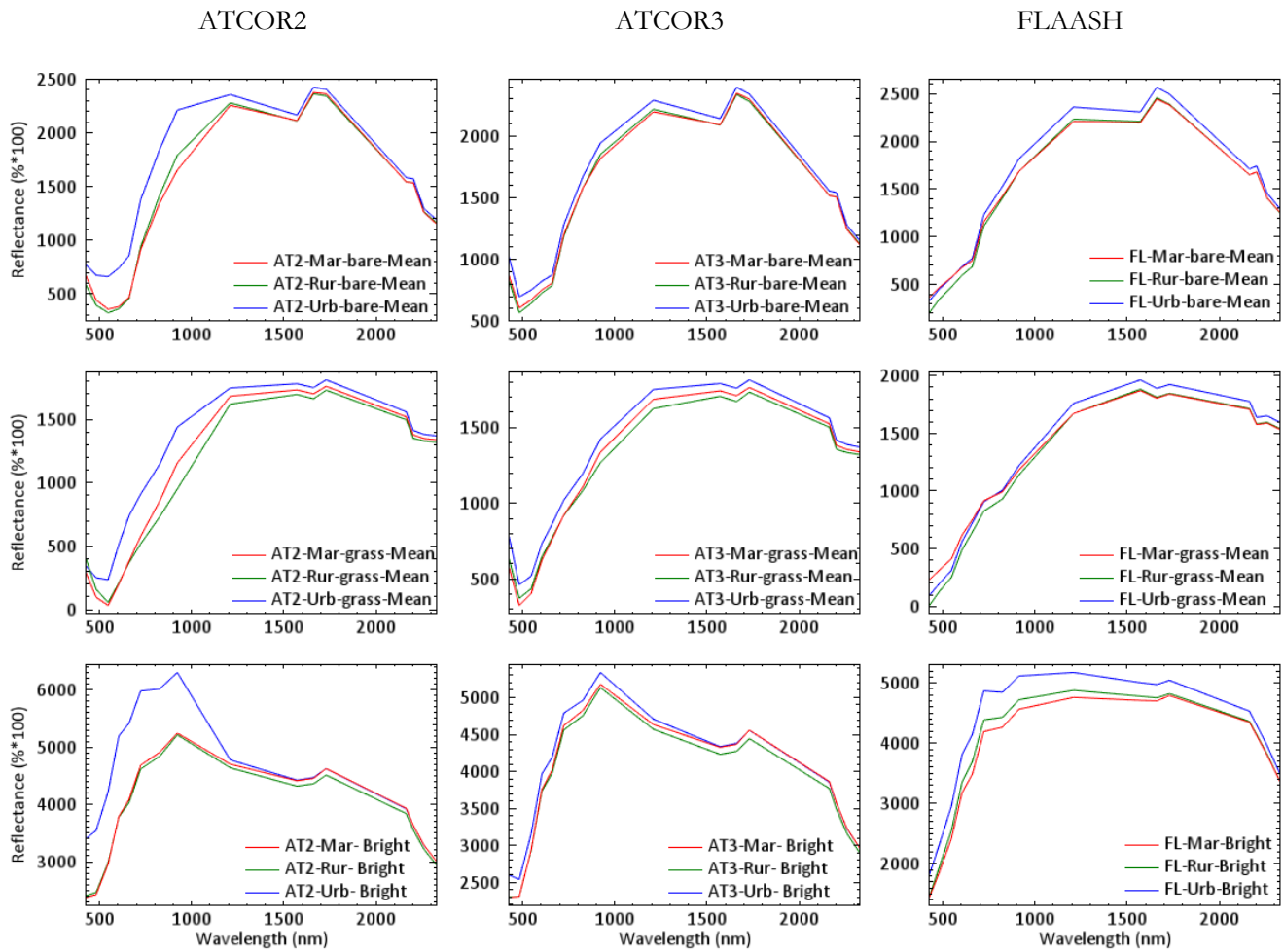
Location map of selected different land cover types. background is True Colour Composite image of WV-3 VNIR data.

Appendix 3. Input parameters of May WV-3 image used for ATCOR and FLAASH methods.

The input parameters used in ATCOR for the May WV-3 image.

Sensor and scene parameters	VNIR	SWIR
Selected Sensor	wv3_vnir 8ch	wv3_swir 8ch
Sensor incidence angle	19.6°	20.3°
Satellite azimuth angle	32°	31.3°
Pixel size	1.2m	7.5m
Solar zenith angle	18.2°	
Solar azimuth angle	143.3°	
Calibration file	Created by automatic metadata import	
Ground elevation	0.15km for ATCOR2 / DEM for ATCOR3	
Atmospheric parameters		
Water vapor category	Mid-latitude summer	
Aerosol type	rural/maritime/urban	
Visibility	40km	

The input parameters used in FLAASH for the May WV-3 image.

Scene and sensor parameters	
Sensor Type	WorldView-3
Sensor altitude (km)	617
Scene center location	36°51'18.81"N; 2°2'13.03"W
Flight date	28-May-2017
Flight time (GMT)	11:19:12
Pixel size (m)	7.5
Ground elevation (km)	0.15
Atmospheric parameters	
Atmospheric model	Mid-Latitude Summer
Aerosol model	Maritime/rural/urban
Initial Visibility (km)	40
Multispectral settings	
KT upper channel	SWIR-5 (2165)
KT lower channel	Red (660.1)
Max.upper.chan.reflectance	0.08
Reflectance ratio	0.5

Appendix 4. Spectral comparison between AComp, ATCOR3, and FLAASH results with field spectra.

The comparison is shown from September image for the Wp333 reference site.